



HAL
open science

An experimental study of dissolution and precipitation of forsterite in a thermal gradient: implications for cellular growth of olivine phenocrysts in basalt and melt inclusion formation

Mickaël Laumonier, Didier Laporte, François Faure, Ariel Provost, Pierre Schiano, Kazuhiko Ito

► To cite this version:

Mickaël Laumonier, Didier Laporte, François Faure, Ariel Provost, Pierre Schiano, et al.. An experimental study of dissolution and precipitation of forsterite in a thermal gradient: implications for cellular growth of olivine phenocrysts in basalt and melt inclusion formation. *Contributions to Mineralogy and Petrology*, 2019, 174, 10.1007/s00410-019-1627-x . hal-02338892

HAL Id: hal-02338892

<https://hal.science/hal-02338892>

Submitted on 30 Oct 2019

HAL is a multi-disciplinary open access archive for the deposit and dissemination of scientific research documents, whether they are published or not. The documents may come from teaching and research institutions in France or abroad, or from public or private research centers.

L'archive ouverte pluridisciplinaire **HAL**, est destinée au dépôt et à la diffusion de documents scientifiques de niveau recherche, publiés ou non, émanant des établissements d'enseignement et de recherche français ou étrangers, des laboratoires publics ou privés.



2 **An experimental study of dissolution and precipitation of forsterite**
3 **in a thermal gradient: implications for cellular growth of olivine**
4 **phenocrysts in basalt and melt inclusion formation**

5 Mickael Laumonier¹ · Didier Laporte¹ · François Faure² · Ariel Provost¹ · Pierre Schiano¹ · Kazuhiko Ito³

6 Received: 6 December 2018 / Accepted: 3 October 2019
7 © Springer-Verlag GmbH Germany, part of Springer Nature 2019

8 **Abstract**

9 The morphology of crystals in magmas strongly depends on the temperature regime of the system, in particular the degree of
10 undercooling and the cooling rate. To simulate low degrees of undercooling, we developed a new experimental setup based
11 on thermal migration, in which large cylinders of forsterite (single crystals) immersed in haplobasaltic melt were subjected
12 to a temperature gradient. As forsterite solubility is sensitive to temperature, the forsterite on the high-temperature side
13 undergoes dissolution and the dissolved components are transported toward the low-temperature side where a layer of newly
14 grown forsterite forms (up to 340 μm thick after 101 h). A striking feature is that the precipitation process does not produce a
15 planar front of forsterite advancing at the expense of liquid: the growth front shows a fingered outline in planar section, with
16 solid lobes separated by glass tubes that are perpendicular to the growth front. We ascribe this texture to cellular growth, a
17 type of growth that had not been experimentally produced so far in silicate systems. We find that the development of cel-
18 lular growth requires low degrees of undercooling (a few °C) and large crystal–liquid interfaces (~1 mm across or more),
19 and that it occurs at a growth rate of the order of 10⁻⁹ m/s. We found natural occurrences of cellular growth on the rims of
20 olivines from basanites, but otherwise cellular textures are poorly documented in natural volcanic rocks. Melt inclusions were
21 produced in our experiments, showing that they can form in olivine at relatively slow rates of growth (10⁻⁹ m/s or lower).

22 **Keywords** Crystal growth and dissolution · Cellular growth · Temperature gradient · Melt inclusion formation · Thermal
23 migration

24 **Introduction**

25 Crystals and melt inclusions are precious tools to decipher the processes from magma production to final emplacement, and they have been the topic of an impressive amount of studies in the past decades. Melt inclusions are parcels of liquid trapped in crystals, which hold precious information on the chemical composition (major and trace elements, volatiles) of primitive magmas (Roedder and Bodnar 1980; Schiano 2003). Zoning patterns, shape and texture of crystals are a record of the composition of the liquid they grew from and the conditions during crystallization (Welsch et al. 2013). To decipher igneous processes, we need to know the growth mechanisms of minerals. The rate at which crystals grow is of particular interest to investigate the timescale of magmatic processes, such as magma ascent rate or crystal residence time in a reservoir prior to eruption (Armienti et al. 1994; Brewer 2000; Murphy et al. 2000; Blundy et al. 2006; Schiano et al. 2006; Humphreys et al. 2006; Morgan

A1 Communicated by Timothy L. Grove.

A2 **Electronic supplementary material** The online version of this
A3 article (<https://doi.org/10.1007/s00410-019-1627-x>) contains
A4 supplementary material, which is available to authorized users.

A5 ✉ Mickael Laumonier
A6 mickael.laumonier@gmail.com

A7 ¹ Université Clermont Auvergne, CNRS, IRD, OPGC,
A8 Laboratoire Magmas et Volcans, 63000 Clermont-Ferrand,
A9 France

A10 ² Université de Lorraine, CNRS, Centre de
A11 Recherches Pétrographiques et Géochimiques,
A12 54501 Vandoeuvre Les Nancy, France

A13 ³ Faculty of Bioenvironmental Science, Kyoto Gakuen
A14 University, Kameoka, Kyoto 621-8555, Japan

and Blake 2006; Castro and Dingwell 2009; Costa et al. 2010; Viccaro et al. 2012; Zellmer et al. 2012; Druitt et al. 2012; Eppich et al. 2012).

Crystal growth is controlled by a dominant rate controlling process that defines the morphology of the crystal. Such processes are reaction at the crystal–melt interface, chemical diffusion in the melt or latent heat flow (Kirkpatrick 1975, 1981; Sunagawa 1981). The reactions at the crystal–melt interface are attachment mechanisms such as continuous growth, surface nucleation or screw dislocation. In this case, there are not significant compositional gradients in the melt along the interface. Diffusion controls the crystal growth when it is slower than attachment mechanisms. Growth controlled by chemical diffusion may produce spatial compositional gradients and usually results in morphologies like skeletal or dendritic crystals. The mechanisms that define the crystal shape and size depend on the variation of extrinsic (temperature, pressure...) or intrinsic (chemical composition, volatile content) parameters. A determinant parameter affecting the mechanism of crystal growth is temperature. In most cases, the increase of the crystal growth rate is attributed to the cooling regime of the magmatic system (O’hara et al. 1968; Takei and Kobayashi 1974; Faure and Schiano 2005). For instance, the olivine growth shape switches from polyhedral, to skeletal and to dendritic with increasing degree of undercooling and cooling rate (Donaldson 1976; Faure et al. 2003a). This crystallization shape sequence does not include cellular growth that produces an intermediate morphology (between polyhedral and skeletal/dendritic) at relatively low growth rates. Cellular growth is well known in metallurgy but poorly documented in silicate minerals (Tiller et al. 1953; Keith and Padden 1963; Shechtman et al. 1984).

Most experimental studies of olivine crystal morphologies were performed at relatively large undercooling degrees and cooling rates (Donaldson 1976; Jambon et al. 1992; Faure et al. 2003a, 2007; Faure and Schiano 2005; Goldstein and Luth 2006), which are specific to scenarios like the emplacement of a small volume of magma at or near the Earth surface. However, the large abundance of dominantly polyhedral olivine phenocrysts in igneous rocks implies low degrees of undercooling and cooling rates in numerous natural magmatic environments. At present, the study of the effect of low undercooling degrees ($\leq 10\text{ }^{\circ}\text{C}$) on crystal growth is nearly absent from the literature due to experimental limitations. To fill this gap, we conducted thermal migration experiments, in which large forsterite crystals immersed into a basaltic liquid were subjected to a low-temperature gradient (typically, 5–10 $^{\circ}\text{C}/\text{mm}$). In the presence of a thermal gradient, solid–liquid systems are known to undergo dissolution–precipitation processes that contribute to mass transport and can strongly affect the development of cumulates in layered intrusions or the compaction

of partially molten rocks (Leshner and Walker 1988; Walker et al. 1988; Schiano et al. 2006; Sonzogni et al. 2011). At a smaller scale, a thermal gradient can cause the migration of a melt inclusion in its host crystal (Leshner and Walker 1988; Walker et al. 1988; Schiano et al. 2006; Sonzogni et al. 2011).

Figure 1 illustrates the concept of thermal migration (Buchwald et al. 1985; Leshner and Walker 1988; Walker and Agee 1988) and how it was adapted in our experimental study. Thermal migration is a process of mass transport and phase redistribution in a mixture of crystals and liquid subjected to a temperature gradient. It comprises two components: chemical diffusion resulting from variations of mineral solubility with temperature, and thermodiffusion (Soret effect) resulting from differences in temperature in the liquid. We consider a simple binary system A–B, with crystals of phase A in suspension in an interconnected liquid phase. If this system is placed in a temperature gradient, then local equilibrium between phase A and liquid will impose a more A-rich liquid composition on the high-temperature side (T^+ in Fig. 1), and a more B-rich composition on the low-temperature side (T^- in Fig. 1). As the liquid is interconnected, this gradient in liquid composition will give rise to chemical diffusion of component A from regions of high temperature to regions of low temperature, and of component B in the opposite direction. This process, which is dictated by local mineral saturation, is called saturation gradient chemical diffusion (Leshner and Walker 1988; Walker and Agee 1988). To maintain local equilibrium between crystals

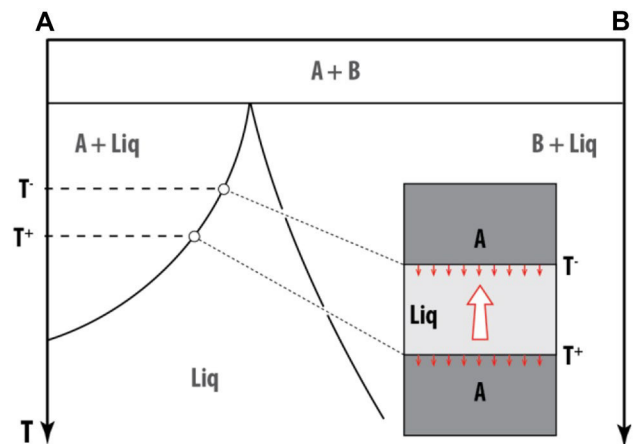


Fig. 1 Illustration of saturation gradient chemical diffusion in a binary system A–B. In contrast to the conventional usage, temperature is increasing downwards to be consistent with the experimental conditions. The sketch on the right shows one of the configurations used to study forsterite growth and dissolution; a thin layer of liquid is placed between two forsterite monocystals in a temperature gradient. The small arrows indicate the displacement of the upper solid–liquid interface (growth front at temperature T^-) and of the lower interface (dissolution front at T^+). The large arrow shows the diffusion of dissolved forsterite components in the liquid

Author Proof

124 and liquid, phase A must continuously dissolve on the high-
125 temperature side and precipitate on the low-temperature
126 side. In parallel to saturation gradient chemical diffusion, the
127 liquid phase will also undergo thermodiffusion. In the case
128 of basic silicate liquids, thermodiffusion leads to the trans-
129 port of dissolved olivine components (MgO, FeO) toward
130 the low-temperature side of the thermal gradient (Leshner
131 and Walker 1986). Accordingly, in our study, Soret effect
132 will assist saturation gradient chemical diffusion and lead
133 to additional concentration of forsterite on the cold end of
134 experimental charges.

135 In comparison to former thermal migration experiments
136 (Leshner and Walker 1988; Walker and Agee 1988; Walker
137 et al. 1988), the main difference in our study is that we
138 replaced the small olivine crystals by large forsterite cyl-
139 inders (single crystals). The most simple configuration is
140 sketched in Fig. 1: it is composed of a thin layer of liquid
141 between two forsterite monocrystals. Because of the differ-
142 ence of temperature, the lower forsterite–liquid interface
143 (at T^+) will continuously dissolve, and the lower forsterite–
144 liquid interface (at T^-) will continuously grow during
145 the experiment. We show that studying the behavior of large
146 monocrystals in a thermal gradient allows to bridge the gap
147 between Ostwald ripening experiments, in which degrees
148 of undercooling are ≤ 1 °C (Cabane et al. 2005), and cool-
149 ing experiments, in which crystal growth data can only be
150 obtained at degrees of undercooling of ≈ 10 °C or more
151 (Donaldson 1976; Kirkpatrick 1981). Another advantage

of our experimental configuration is to provide at the same
time an insight into the dissolution and crystallization pro-
cesses at low degrees of superheating and undercooling,
respectively.

Experimental procedure

Starting materials and experimental protocol

The experiments were run in the simplified system
 $\text{Na}_2\text{O}-\text{CaO}-\text{MgO}-\text{Al}_2\text{O}_3-\text{SiO}_2$ (Na-CMAS). The hap-
lobasaltic glass was produced by Schott AG Company (see
chemical compositions in Table 1) and crushed down into
fine powder. Cylinders of forsterite 2–2.5 mm diameter were
cored in a large synthetic monocrystal of pure Mg_2SiO_4 (Ito
et al. 2003a, b) (Table 2). The thickness of the forsterite cyl-
inders ranged from 0.6 to 2.3 mm. The faces of the cylinders
were polished down to the micron. The starting materials
were loaded in platinum capsules with an outer diameter
of 3.0 mm and an inner diameter of 2.6 mm. The capsules
were inserted into an assembly for a 3/4-inch piston–cylinder
apparatus with Pyrex glass and NaCl sleeves used as pres-
sure medium and thermal insulator. All experiments were
conducted at 10 kbar (1 GPa) and 1400 or 1425 °C (Table 3).
The temperature was generated by a graphite cylinder and
read by a C-type (tungsten–rhenium alloy) thermocouple
placed about 0.8 mm below the capsule. Prior to experiment,

Table 1 Electron probe microanalyses of the glass (2σ)

Exp.#	Location (number of analyses)	SiO ₂	Al ₂ O ₃	MgO	CaO	Na ₂ O	Total	An
Synthesis ^a	Starting glass (54)	49.25	19.41	16.4	12.83	2.11	100	0.77
		0.46	0.25	0.25	0.25	0.12	0.68	0.01
A4	Bath at the top (12)	49.52	17.63	19.18	11.80	1.87	100.34	0.78
		0.29	0.56	0.36	0.33	0.18	0.76	0.02
	Between pillars (32)	49.53	17.58	19.16	11.83	1.90	100.36	0.78
		0.22	0.56	0.48	0.31	0.15	0.91	0.01
Bottom (17)	49.30	17.88	18.91	11.96	1.95	100.14	0.77	
	1.96	1.65	1.95	0.54	0.20	1.89	0.01	
B6	Middle (78)	49.34	18.84	17.32	12.42	2.07	99.73	0.77
		0.38	0.41	0.82	0.52	0.17	1.23	0.02
	Top cyl. (23)	49.11	19.48	16.81	12.41	2.18	99.60	0.76
		0.56	0.47	0.35	0.32	0.12	0.83	0.01
<i>Melt inclusions</i>								
A2	Euhedral Fo, Fig. 6c (5)	50.32	22.96	8.53	13.51	2.89	98.20	0.72
		0.56	0.48	0.20	0.74	0.36	0.84	0.02
A4	Overgrowth, Fig. 7c, d (5)	50.96	21.32	10.33	14.25	2.35	99.20	0.77
		0.28	0.32	0.12	0.26	0.20	0.20	0.02
B1	Overgrowth, Fig. 5b (5)	49.17	19.99	13.84	14.24	2.06	99.31	0.79
		0.84	0.67	1.18	0.42	0.26	0.58	0.01

^aFrom M. Hardiagon (unpublished data)

^bAnorthite content An is the Ca/(Ca + Na) molar ratio

Author Proof

Table 2 Electron probe microanalyses of the different types of forsterite (2σ): the cores of the monocrystalline cylinders; the overgrowth layers on the forsterite cylinders; the pillars on the dissolution side of the cylinders; the large euhedral forsterites that grew during the experiments; the small forsterite grains in suspension (“Fo bath”)

Location	Exp.# (number of analyses)	SiO ₂	Al ₂ O ₃	MgO	CaO	Na ₂ O	Total	Mg/Si (Fo)
Cylinder core	Starting (8)	42.83 0.45	0.02 0.03	57.15 1.04	0.00 -0.01	0.00 0.01	100.76 1.22	1.99 0.04
	A0 (6)	42.46 0.55	0.01 0.02	57.52 0.47	0.01 0.01	0.01 0.02	100.77 0.84	2.02 0.03
	A4 (46)	42.82 0.66	0.02 0.03	57.13 0.66	0.01 0.03	0.01 0.02	101.18 1.22	1.99 0.01
	B6 (48)	42.62 0.63	0.01 0.02	57.34 0.62	0.01 0.04	0.00 0.01	99.10 1.06	2.01 0.05
Cylinder overgrowth	A4 (8)	43.21 0.40	0.13 0.08	56.41 0.66	0.24 0.13	0.01 0.03	101.80 0.72	1.95 0.03
	B6 (14)	42.63 0.32	0.13 0.08	56.96 0.34	0.28 0.10	0.01 0.02	99.02 0.69	1.99 0.03
Cylinder pillars ^a	A4 (1)	42.87	0.05	56.96	0.12	0.01	101.30	1.98
	B6 (1)	42.49	0.03	57.35	0.13	0.00	99.38	2.00
Euhedral Fo	B6 (16)	42.56 0.68	0.14 0.04	57.00 0.69	0.28 0.04	0.01 0.03	99.23 0.61	2.00 0.05
Fo bath	A4 (9)	42.73 0.32	0.14 0.04	56.84 0.36	0.28 0.03	0.02 0.04	100.22 0.61	1.98 0.03

^aRepresentative compositions of the inner part of the pillars (analyzed at 15–20 μm from the liquid)

Table 3 Summary of experimental conditions

Exp ^a	m Fo	Fo axis ^b	m bath	m Fo/m bath	Fo/gl	Height (mm) Fo1; Fo2	T °C ^c	Duration (h)	Phases
A0	12.8	<i>a</i> -axis	25.8	0.33	0.55	1.02	1425	0.1	gl, ol
A2 ^d	31.2	<i>a</i> -axis	27.0	0.54	0.69	2.19	1400	176.0	gl, ol, cpx, sp
A4	29.8	<i>a</i> -axis	36.4	0.45	0.63	2.10	1425	48.1	gl, ol
B1 ^d	11.7	<i>a</i> -axis	34.5	0.25	0.25	0.68; 0.58	1425	45.2	gl, ol, sp
B6	32.0	<i>a</i> -axis	16.0	0.67	0.78	0.86; 1.41	1400	101.0	gl, ol
B7	28.6	<i>b</i> -axis	14.8	0.66	0.77	1.05; 0.94	1400	50.4	gl, ol
B8	47.1	<i>c</i> -axis	15.4	0.75	0.83	1.75; 1.53	1400	47.6	gl, ol
B9	33.9	<i>a</i> -axis	15.5	0.69	0.79	1.24; 1.11	1400	22.9	gl, ol

^aIn type A experiments, a single forsterite cylinder was immersed into a mixture of glass (67 wt%) plus small forsterite grains (33 wt%). In type B experiments, a glass layer was placed between two forsterite cylinders (Fo1 is the upper cylinder; Fo2 the lower cylinder)

^bMost cylinders were drilled along the *a*-axis of the forsterite lattice, except those in run B7 (parallel to *b*-axis) and in run B8 (parallel to the *c*-axis); see Fig. S2

^cThermocouple temperatures: the temperatures at the hot post are about 20 °C higher than these temperatures (see Fig. S1)

^dNo Au–Pd sputtering

m Fo mass of forsterite in mg, *m bath* mass of the bath (glass or glass + small forsterite) in mg, *height* height of the forsterite cylinder(s), *phases* phases present in the run products (gl, glass; ol, olivine; cpx, clinopyroxene; spl, spinel)

176 the assemblage containing the capsule was stored at 150 °C
 177 for 12 h minimum. The experiments started with the pres-
 178 surization of the assembly to 3–4 kbar to ensure good elec-
 179 trical contacts between the graphite furnace and the power
 180 supplier without fracturing the solid pieces of the assembly.
 181 Then the temperature was raised to 650 °C (close to the

Pyrex glass transition) with a rate of 60 °C/min and kept
 constant for the end of the pressurization of the assembly.
 Once close to the target pressure (10 kbar), the temperature
 was increased to the desired set point (1400 or 1425 °C) and
 maintained constant during the experiment by a Eurotherm
 controller. Run duration ranged from 0 to 176 h. At the end

182
183
184
185
186
187

188 of the experiment, the sample was quenched by switching off
189 the power, resulting in a cooling rate of ~ 80 °C/s, and then
190 slowly decompressed to 1 bar. Details of the experimental
191 conditions are presented in Table 3.

192 Setup geometry

193 In our experiments, a system composed of forsterite
194 monocrystal(s) in contact with a haplobasaltic melt is sub-
195 jected to a temperature gradient. In a first series of experi-
196 ments, we used the experimental configuration A, in which
A02 a single forsterite crystal (Fig. 2a) about 1–2 mm thick is
198 immersed in haplobasalt. In the final series, we used the
199 configuration B, in which a liquid layer of the order of mm
200 is sandwiched between two crystals (Figs. 1, 2b). Based on
201 temperature calibration experiments, we adjusted the posi-
202 tion of the capsule into the piston–cylinder assembly so that
203 its bottom was less than 1 mm below the hot spot in every
204 experiment (Figs. 2 & S1). Consequently, most of the cap-
205 sule (70–80%) was above the hot spot and was subjected to
206 a temperature decreasing upwards.

207 The principle of our thermal migration experiments is
208 best explained by considering configuration B (Figs. 1, 2b).
209 In type B experiments, the opposite faces of the cylinders
210 are at temperatures T^+ (upper face of lower cylinder) and
211 T^- (lower face of the upper cylinder), with $T^+ > T^-$. Let us
212 assume that the liquid is homogeneous at the beginning,
213 with a composition in equilibrium with forsterite at the mean
214 temperature $(T^+ + T^-)/2$. As forsterite solubility depends on
215 temperature, the liquid is slightly oversaturated in forsterite
216 on the colder side of the liquid layer, and undersaturated on
217 the hotter side. This situation triggers a process of forsterite
218 dissolution, transport, and precipitation. The driving force is

219 proportional to the temperature difference $\Delta T = T^+ - T^-$, and
220 we assume that the degree of undercooling along the upper
221 face of the monocrystal and the degree of superheating on
222 the lower face are equal to $\approx \Delta T/2$. Thus, for a thermal gra-
223 dient of 6 °C/mm (typical of type B experiment; see below)
224 and a melt thickness of 1 mm, the degree of undercooling
225 driving forsterite growth will be 3 °C. Type B configuration
226 provides a straightforward path for solute transport from the
227 dissolution site to the precipitation site (Fig. 1).

228 In theory, the same reasoning applies to experimental
229 configuration A (Fig. 2a), with a difference of temperature
230 between the lower face of the forsterite monocrystal and its
231 upper face equal to the thermal gradient times the thick-
232 ness of the monocrystal. In this case, we expected the lower
233 face of the forsterite to dissolve, the dissolved components
234 to be transported upwards (in the thin melt layer between
235 the forsterite and the platinum wall), and the upper face of
236 the forsterite to crystallize. In practice (see “Results”), we
237 observed that at the end of type A experiments, the plati-
238 num capsule was pressed against the forsterite monocrystal
239 and that there was almost no melt layer left to transport the
240 dissolved forsterite components upwards. Hence, the upper
241 and lower parts of the sample behaved as two independent
242 subsystems in all type A experiments.

243 Sample preparation

244 In type A geometry (runs A0, A2 and A4; Fig. 2a; Table 3),
245 the sample was composed of a forsterite cylinder embedded
246 in a mixture of haplobasaltic glass and small grains of forst-
247 erite (33 wt% forsterite/67 wt% glass). The purpose of add-
248 ing micron-sized grains of forsterite in type A experiments
249 was to ensure a fast establishment of equilibrium between

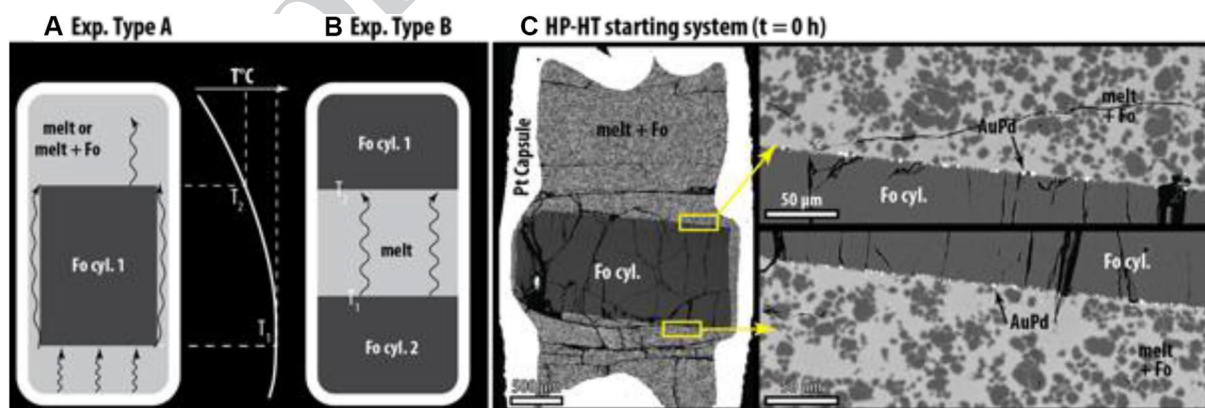


Fig. 2 Sketch of the experimental geometries used for experiments of types A (a) and B (b), with a typical qualitative temperature (T) distribution along the capsule axis; the hot spot is located in the lower third of the capsule, 0.5–0.7 mm above the bottom. The height of the samples ranges from 3.1 to 5.1 mm. c Experiment A0 at time zero ($t=0.1$ h; Table 3); SEM picture of the whole sample and enlarge-

ments of the upper and lower faces of the forsterite cylinder; the matrix is composed of small grains of forsterite and Na–CMAS basaltic glass. The bright small balls are metallic droplets produced by the destabilization of a thin layer of $\text{Au}_{80}\text{Pd}_{20}$ sputtered on the faces of the forsterite cylinder

forsterite and liquid at the beginning of the experiments. In type B geometry (runs B1, B6–9; Fig. 2b), a layer of pure haplobasaltic glass was sandwiched in between two forsterite cylinders.

In all type A experiments and in experiments B1, B6 and B9, the cylinders were drilled along the *a*-axis of the forsterite lattice (i.e., perpendicular to (*b*, *c*) plane; see Fig. S2). Some cylinders were prepared differently to explore the effect of crystal orientation on growth mechanisms: cylinders of run B7 were prepared parallel to *b*-axis, and those in B8 were drilled along the *c*-axis of the starting forsterite single crystal (Fig. S2). The others axes of the cylinders were not constrained due to free rotation during their insertion in the capsule.

The faces of forsterite cylinders can advance or recede several hundred microns during an experiment due to precipitation or dissolution, respectively. To measure precisely these displacements, it is necessary to be able to locate the initial position of the forsterite faces. We used a Denton Vacuum Coater to sputter the planar surfaces of each forsterite cylinder with a layer of Au₈₀Pd₂₀ (except in two experiments, B1 and A2, to compare the dissolution and growth textures with and without gold–palladium sputtering). At run temperature, the thin layer (a few tens of nanometers) decomposes into an array of coplanar droplets, which mark the original surfaces without disturbing the dissolution and precipitation processes (Fig. 2c). The decomposition of the continuous Au–Pd layer into droplets is due to the fact that the experiments are run well above the melting temperature of the alloy and that when the alloy layer melts, it breaks down into droplets to minimize interfacial energy.

Thermal profile

Our experiments were conducted at constant temperature, the main driving force for forsterite growth and dissolution being the temperature difference along the sample height. In a piston–cylinder assembly, the temperature difference between the top and the bottom of a sample depends on its vertical position relative to the hot spot of the furnace (Fig. 2a). The thermal profile along the axis of our piston–cylinder assemblies has been calibrated previously using either multiple temperature readings (up to five) at different heights or the reaction $\text{MgO} + \text{Al}_2\text{O}_3 \rightarrow \text{spinel}$ (Watson et al. 2002) (Fig. S1). These calibrations show that the position of the hot spot is rather well constrained: it is at 17 ± 0.5 mm from the basis of the assembly, with values closer to 16.5 mm at high temperatures (1200 °C and above). This is about the mid-height of the furnace (34.3 mm high, including a 1.3-mm-thick graphite disc at the top). In our experimental configuration, the thermocouple tip is located at a height of 14.5 mm, that is about 2 mm below the hot spot, and the temperature difference between the thermocouple

and the hot spot is 20 °C (note that the temperatures in Table 3 are the thermocouple temperatures; Fig. S1). There is a thin alumina disc separating the thermocouple tip and the platinum capsule, and the bottom of the silicate sample is located 0.5–0.7 mm below the hot stop (depending on the thickness of the platinum weld at the bottom of the capsule).

To estimate the temperature at the top of the capsules (the low-temperature side, on the opposite side to the thermocouple tip), we relied on two independent techniques: (1) the temperature calibration curve in Fig. S1, and (2) the appearance of secondary mineral phases (spinel and clinopyroxene) using the phase diagram of our CMAS–Na haplobasaltic composition as reference (M. Hardiagon, personal communication). At 10 kbar, the liquidus temperature lies between 1450 and 1425 °C, and the liquidus phase is forsterite (Fo). The second solid phase that crystallizes at 10 kbar is spinel (Sp), which appears between 1400 and 1375 °C, and the third one is clinopyroxene (Cpx), which appears between 1350 and 1300 °C. At 1300 °C, Cpx and plagioclase (Pl) are stable, in addition to Fo and melt, while spinel is absent. To compute the temperature difference between the bottom and the top of the samples, we considered that the Spl- and Cpx-in temperatures are equal to $1385 (\pm 10 \text{ °C})$ and $1330 (\pm 20 \text{ °C})$, respectively.

The thermal data are summarized in Table 4. The temperature difference between the warmest and the coldest regions of a capsule ranges from 20 to 80 °C depending on the length of the capsule. The 80 °C difference corresponds to experiment A2, which was the one with the longest capsule (5.1 mm); it is the only one in which Cpx was found at the top of the capsule (see below). The temperature difference between the two faces of a forsterite cylinder in type A experiments ranges from 8 to 25 °C, depending on their thickness and position in the capsule. The melt layer in type B experiments is placed about 1 mm above the hot spot; thus, the temperature difference across the glass layer between the two forsterite cylinders is less than ~10 °C and the thermal gradient is typically 5–6 °C/mm (Fig. S1), except in B1 (10 °C/mm) because the capsule was longer.

Analytical techniques

At the end of an experiment, the whole platinum capsule was mounted in epoxy, sectioned lengthwise, polished and carbon coated. Textures of the experimental products were observed with a JEOL JSM-5910 LV scanning electron microscope (SEM). Crystal fractions and sizes were determined from SEM photographs of 2D sections (automatic threshold based on the gray level) using SPO2003 software (Launeau 2004). Crystal orientation and face recognition were done from interfacial angle measurements following Welsch et al. (2013). Chemical analyses of the run products were made by electron probe microanalysis (EPMA)

Table 4 Main characteristics of experimental products

Exp#	Thickness ^a cylinder 1		Thickness ^a cylinder 2		Temperature		Ratio Fo1	Ratio Fo2	Bulk ratio	Sample height (mm)	Dif-ference ^b (sample)	Average gradient ^b (°C/mm)	Cylinder 1			Euohedral Fo growth ^e		
	Before	After	Before	After	Dissolution ^c	Thick. (mm)							Rate (m/s) × 10 ¹⁰	Thick. (mm)	Rate (m/s) × 10 ¹⁰	Size (mm)	Rate (m/s) × 10 ¹⁰	
																		Growth ^d
A0	1.01	1.00			0.99	0.99			0.99	5.07	80	15.8	0.33	5.3	0.31	5.0	0.13	2.1
A2	2.14	2.12			0.99	0.99			0.99	4.45	45	10.1	0.19	10.7	0.20	11.3	0.05	2.9
A4	2.10	2.11			1.00	1.00			1.00	4.48	45	10.0	0.12	7.4	0.20	12.3	0.10	6.2
B1	0.68	0.76	0.58	0.36	1.12	0.62	0.62	0.89	0.89	3.43	20	5.8	0.33	9.1	0.34	9.4	0.19	5.2
B6	0.86	0.83	1.41	1.18	0.97	0.84	0.84	0.89	0.89	3.11	20	6.4	nd	nd	0.11	6.3	0.06	53.3
B7	0.99	nd	1.08	nd	nd	nd	nd	0.92	0.92	4.27	20	4.7	nd	nd	0.17	10.1	0.07	4.1
B8	1.57	1.52	1.71	1.51	0.97	0.88	0.88	0.92	0.92	3.33	20	6.0	nd	nd	nd	nd	0.06	6.7
B9	1.15	1.11	1.28	1.18	0.97	0.92	0.92	0.94	0.94									

^aThicknesses before and after the experiments were measured with calipers and from SEM image, respectively. In type A experiments, there is only one cylinder (no. 1); in type B experiments, cylinder 1 is the upper forsterite cylinder and cylinder 2 the lower one

^bTemperature differences (from bottom to top) and temperature gradients in absolute values; temperatures are decreasing upwards

^cThe column "Dissolution" gives the thickness of forsterite dissolved and the rate of dissolution. The thickness of forsterite dissolved is equal to the initial cylinder thickness plus the thickness of the growth layer minus the final cylinder thickness

^dThe column "Growth" gives the thickness of the growth layer (equal to the distance from the alignment of Au-Pd droplets to the growth front) and the rate of growth

^e"Size" corresponds to the radius of the largest euohedral crystals

352 using a Cameca SX 100. Analytical conditions were focused
 353 beam (< 1 μm)—15 nA and 22 kV for crystals—and unfocused
 354 beam (< 15 μm)—8 nA and 15 kV for glasses—dur-
 355 ing 10 + 20 + 10 s (background, sample, background). The
 356 probe was calibrated using wollastonite, corundum, albite
 357 and forsterite standards.

358 Results

359 The textural results are illustrated in Figs. 3, 4, 5, 6, 7, and
 360 supplementary Figures S3 and S4. In all figures, the polarity
 361 of the sample during the experiment is respected (that is, the
 362 lower part of the microphotograph corresponds to the bottom
 363 of the sample in the hot spot). The location of electron probe
 364 microanalyses is shown using the same shape and color

codes in Figs. 3, 4, 5, 6, and 7. If we put aside experiment
 A0 that was quenched shortly after heating, major changes
 in the thickness of the forsterite cylinders and in the shape
 of their surfaces occurred during all experiments due to dis-
 solution and precipitation processes.

Dissolution and precipitation textures: type B experiments

Experiments B6–B9 (Figs. 3, 4, S3–S4) show the evolu-
 tion of type B geometry with increasing duration (at
 T = 1400 °C). This geometry is designed to produce a dis-
 solution/precipitation process in three steps (Fig. 1): (1) dis-
 solution of the upper face of the lower cylinder, which is at
 a higher temperature; (2) solute transport upwards through
 the melt layer; (3) precipitation along the lower face of the

B6 - 1400°C - 101h

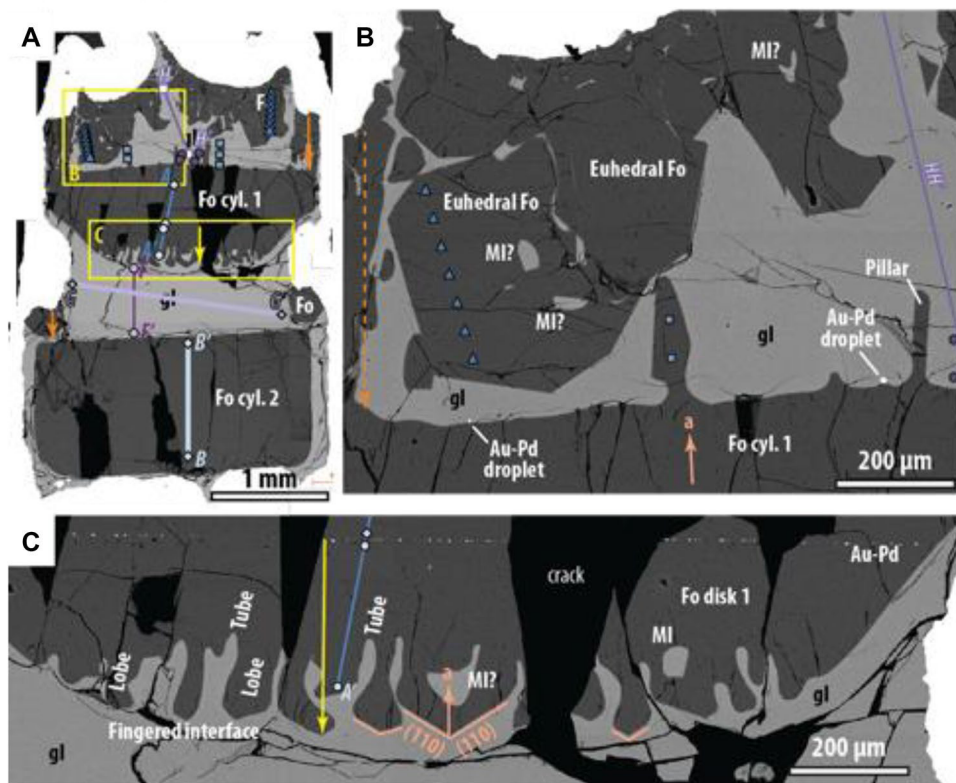


Fig. 3 SEM photographs of experiment B6 (1400 °C, 101 h). **a** Overview of the sample at low magnification. Black regions are due to decompression cracks and crystal snatching, white areas are the platinum capsule, and bright and dark gray are glass (gl) and forsterite (Fo), respectively. **b** Enlargement of the upper part of the sample showing dissolution of the upper face of forsterite cylinder 1 and crystallization of large euhedral forsterite hosting melt inclusions (MI). The dissolution of the upper part of the cylinder is indicated by the Au–Pd droplets deposited on its surface and by the gap between the glass–cylinder interface and the capsule shrinkage (dashed orange arrow). The *a*-axis direction is indicated by an arrow. **c** Enlargement

of the lower face of the upper forsterite cylinder experiencing crystallization. The alignment of bright metallic droplets (Au–Pd) marks the initial forsterite cylinder surface, allowing the determination of the cylinder overgrowth (yellow arrow). Symbols and segments are EPMA spots and chemical profiles, respectively (see Figs. 8, 9). In this figure and the following ones, the polarity of the sample during the experiment is respected; the upper part of the microphotograph corresponds to the top of the sample. Crystal orientation in (C) was determined from interfacial angles indexation following (Welsch et al. 2013)

B8 - 1400°C - 48h

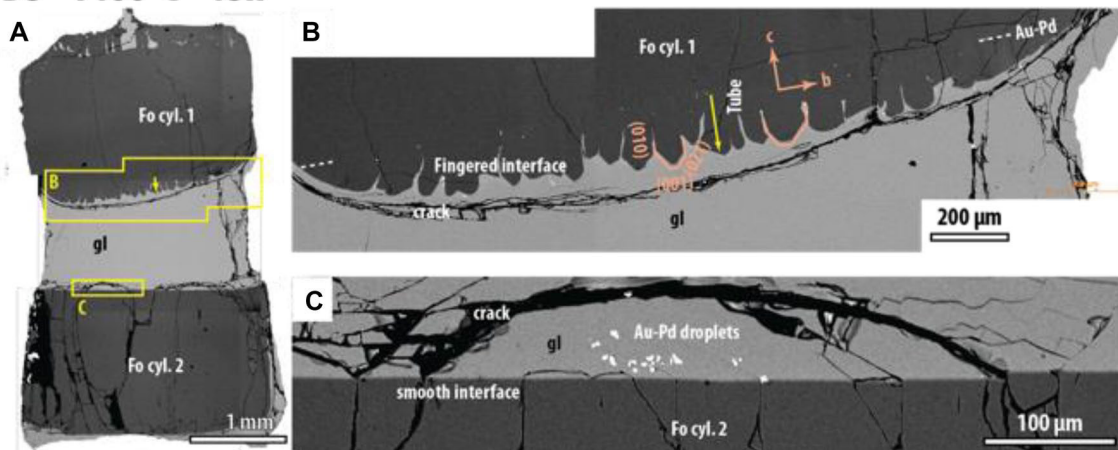


Fig. 4 SEM photographs of experiment B8 (1400 °C, 48 h). **a** Overview of the sample at low magnification. **b** Enlargement of the lower face of the upper forsterite cylinder, showing the fingered outline of the forsterite–liquid interface; the yellow arrow gives the thickness of

the precipitated layer. **c** Enlargement of the upper face of the lower forsterite cylinder: the receding surface is almost perfectly flat. There are some Au–Pd droplets suspended in the glass or fallen on the forsterite surface

379 upper cylinder (at a lower temperature). The most obvious
380 textures are those associated with step (3), especially after
381 101 h and 48 h (Figs. 3c, 4b). In these figures, an alignment
382 of Au–Pd droplets is visible deep inside the forsterite cyl-
383 nder: it corresponds to the Au–Pd layer that was sputtered
384 on the original surface. The thickness of the precipitated
385 layer (measured from the alignment of Au–Pd droplets to
386 the forsterite front) measures 170 μm after 48 h and 340 μm
387 after 101 h. As presented below, the alignment of Au–Pd
388 droplets corresponds also to a compositional limit (for minor
389 elements: Al, Ca) between the starting synthetic forsterite
390 and the newly grown forsterite.

391 A striking feature is that the precipitation process does
392 not produce a planar front of forsterite advancing at the
393 expense of liquid. There is a kind of self-organization that
394 develops, in which domains of faster growth give rise to
395 forsterite lobes protruding into the liquid. As a result, the
396 growth front shows a fingered outline in two dimensions
397 (2-D), with solid lobes separated by tubes of glass that are
398 roughly perpendicular to the growth front (Figs. 3c, 4b).
399 The average lobe spacing is of the order of 0.1 mm (that
400 is, 10 lobes per mm of interface). The longest tubes can be
401 up to ~150 μm deep, but are still shorter than the growth
402 layer (that is, they do not reach the alignment of Au–Pd
403 droplets). The lobes are elongated parallel to the orienta-
404 tion of the forsterite cylinder: parallel to *a*-axis in run B6
405 and parallel to *c*-axis in run B8. Facets controlled by the
406 crystallographic orientation of the cylinder develop at the
407 growth front (Figs. 3c, 4b, S3C and S4B); in Fig. 3c, these
408 crystallographic facets join to form pyramids with sharp
409 edges. In some cases, neighboring lobes merge at their ends
410 and thus entrap melt in the observed section. We checked

by optical microscopy that some of these regions of trapped
melt in 2-D are real glass inclusions in 3-D (i.e., inclusions
totally closed).

As expected, the upper face of the lower cylinder receded
due to dissolution. This is not obvious at first glance because
it remained almost flat (Figs. 3a, 4c, S3A, S4C). In experi-
ment B9 (23 h; Fig. S4C), the slightly curved alignment of
Au–Pd droplets visible in the glass few tens of μm above
the forsterite cylinder demonstrates that the upper part of
the lower cylinder has been dissolved. The Au–Pd align-
ment is no longer visible in the longer duration experiments,
but there are still a few larger Au–Pd droplets visible either
suspended in the glass or fallen on the receding forsterite
surface (Fig. 4c). The dissolution of the lower cylinder is
also demonstrated by the downward displacement of the
upper surface compared to its initial position marked by the
shrinkage of the capsule (displayed by an orange arrow on
Fig. 3a). This shrinkage is due to a higher degree of compac-
tion of glass powder compared to forsterite cylinder during
the compression at the beginning of the experiment. Finally,
the forsterite right below the receding surface has levels of
CaO and Al₂O₃ recalling those in the starting synthetic for-
sterite and lower than those expected at equilibrium with the
haplobasaltic melt (see below).

In our first type B experiment (B1), we used a slightly
different initial configuration, including forsterite cylinders
with a smaller outer diameter (2 mm instead of 2.5 mm).
Figure 5a shows that this configuration was not stable and
that the upper forsterite cylinder fell into the lower part of
the liquid reservoir. We observe, however, the same textures
as above: dissolution along the top of the lower cylinder
produced a flat surface and rounded cylinder edges, and

B1 - 1425°C - 45h

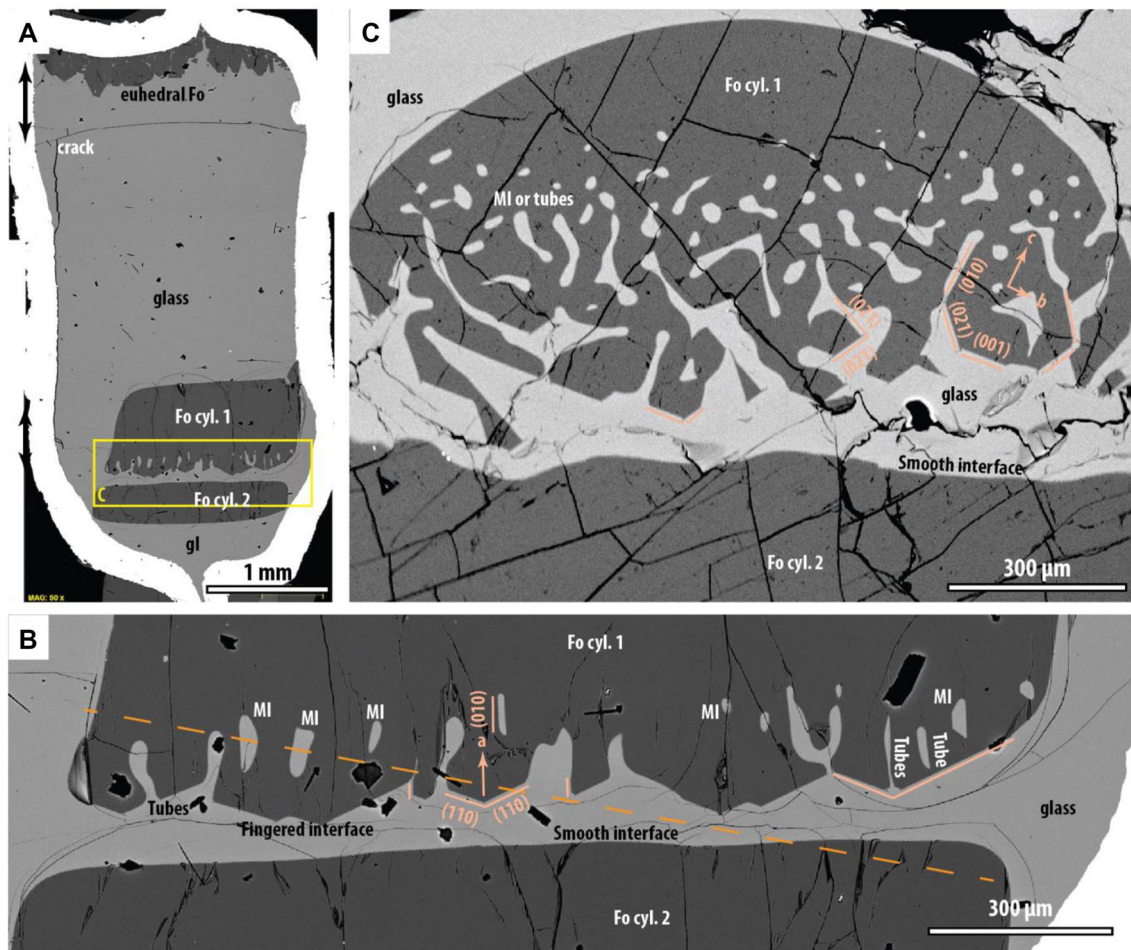


Fig. 5 SEM photographs of experiment B1 (1425 °C, 45 h). **a** Overview of the sample at low magnification, showing the two cylinders at the bottom and a layer of large euhedral forsterite (with a few small spinel crystals) at the top. **b** Enlargement showing precipitation microtextures on the lower face of the upper forsterite cylinder, and

the flat dissolution surface on the top of the lower cylinder. Note the planar facets at the ends of the forsterite lobes and the melt inclusions (MI) and tubes. The orange dashed line corresponds to the position of the cross section shown in **c**. **c** Cross section through the growth front on the lower side of the upper forsterite cylinder

443 precipitation at the base of the upper cylinder yielded a fingered interface, with glass tubes separating solid lobes terminated by crystallographic facets (110) (Fig. 5b). The melt inclusions are especially well developed in this experiment, reaching up to 80 μm and showing a range of shapes from rounded, to ovoid, to negative crystals. A section perpendicular to the growth front is illustrated in Fig. 5c. On a technical point of view, it is interesting to note that experiment 450 451 B1, in which the forsterite cylinders were not sputtered with Au–Pd, shows the same microtextures as in experiments 452 453 with Au–Pd-sputtered forsterite cylinders. Accordingly, the precipitation and dissolution processes are not affected by the presence of droplets of gold–palladium.

456 Unlike the sketch in Fig. 2b, some of the liquid was able to sneak above the upper cylinder during type B experiments 457 (and to a lesser extent under the lower forsterite cylinder). 458

As a result, a second dissolution–precipitation cell operated at the top of the capsule, as a parallel system. The effect is best visible in experiment B6 (Fig. 3), with the recession of the upper face of the top forsterite cylinder and the growth of large euhedral crystals of forsterite hanging from the roof of the capsule. The dissolution of the upper face left a few vertical pillars of forsterite standing several hundreds of microns above a slightly wavy floor (on the right of Fig. 3b). These special features are best visible in type A experiments and will be discussed below.

Dissolution and precipitation textures: type A experiments

A major complication arose in runs A2 (1400 °C, 176 h; Fig. 6) and A4 (1425 °C, 48 h; Fig. 7) due to the absence of

A2 - 1400°C - 176h

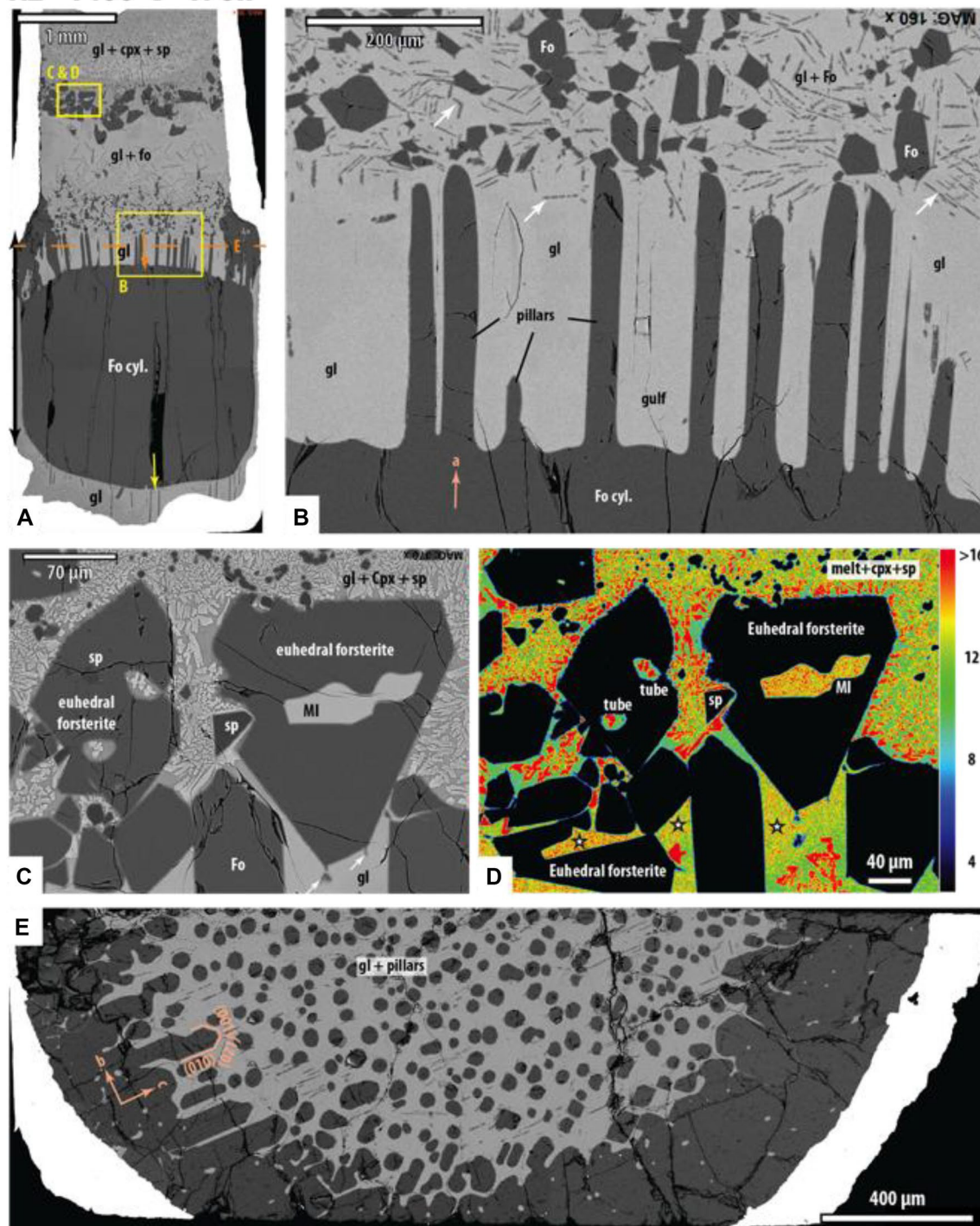
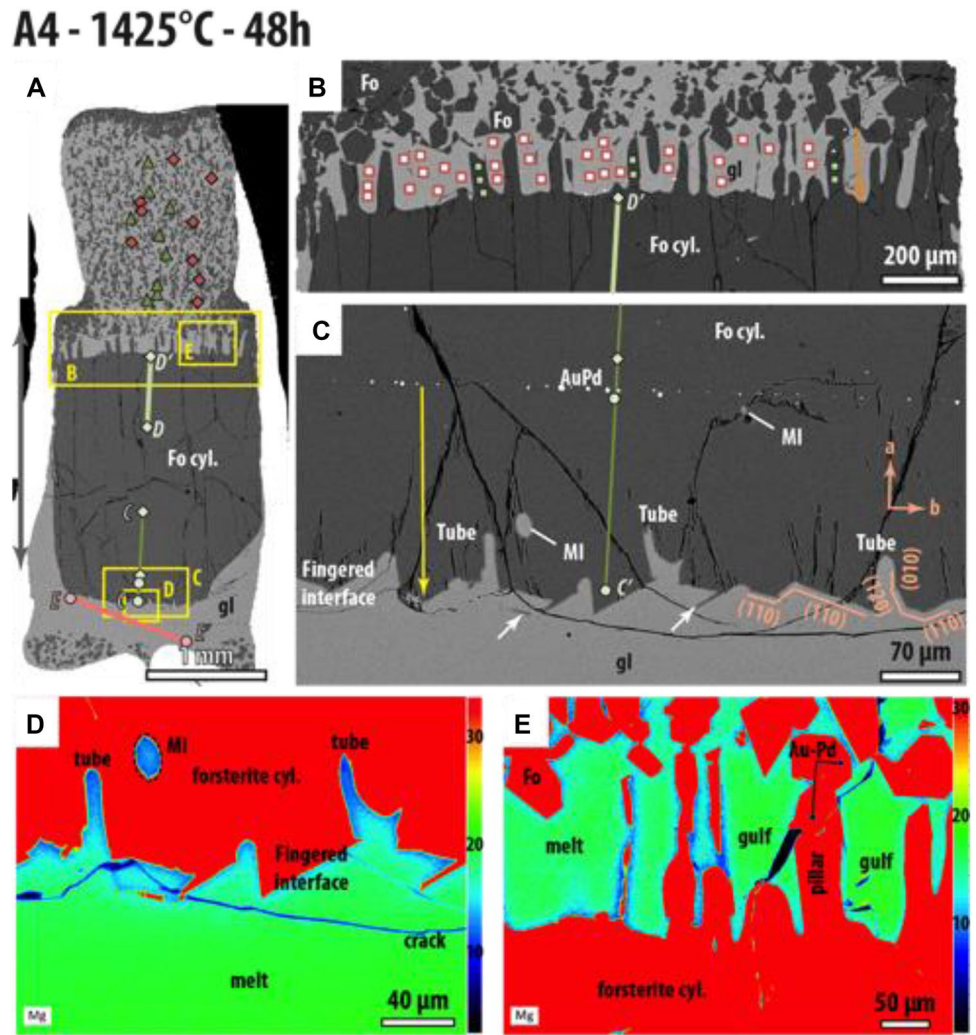


Fig. 6 SEM photographs of experiment A2 (1400 °C, 176 h). **a** Overview of the sample at low magnification showing its mineralogical stratification. The orange arrow shows the thickness of forsterite dissolved on the upper side of the cylinder; the kinks in the platinum wall mark the initial position of the upper surface of the forsterite cylinders before dissolution. The yellow arrow indicates the thickness of forsterite precipitated on the lower side. The orange dashed line corresponds to the position of the cross section shown in (E). **b** Close-up view of the upper part of the forsterite cylinder: pillars of residual for-

sterite stand several hundreds of microns above the receding surface; note the small grains of forsterite suspended in glass above the dissolution zone. The forsterite dendrites (white arrows) presumably grew during quench. **c** SEM micrograph (back-scattered electrons) of large euhedral forsterite in the upper part of the capsule. **d** Calcium map of the same area (with concentration scale in wt% CaO on the right). **e** Cross section through the layer of forsterite pillars and glass in **b**. *Sp* spinel, *Cpx* clinopyroxene, *Fo* forsterite, *gl* glass, *MI* melt inclusion

Fig. 7 SEM photographs of experiment A4 (1425 °C, 48 h). **a** Overview of the sample at low magnification. **b** Close-up view of the dissolution texture at the top of the forsterite cylinder, with pillars of residual forsterite almost 200 μm high. Small grains of forsterite are suspended in the glass above the dissolution zone. **c** Close-up view of the precipitation layer at the bottom of the forsterite cylinder; the layer of Au–Pd droplets is well visible. White arrows: quench overgrowths. Symbols and segments are EPMA spots and chemical profiles, respectively (see Figs. 8, 9). **d** Chemical map of magnesium in part of image (c). **e** Chemical map of magnesium in part of image (b)



473 connection or the poor connection between the lower face of
 474 the forsterite cylinder and its upper face. As a result, the sys-
 475 tem did not work as sketched in Fig. 2A because two inde-
 476 pendent subsystems developed in the lower half and upper
 477 half of capsules. In the lower half, the lower face of the
 478 forsterite cylinder grew at the expense of the small forsterite
 479 grains at the bottom of the capsules, giving rise to crystal-
 480 free layers right below the forsterite cylinder (Figs. 6a, 7c).
 481 Forsterite overgrowth is best visible in run A4 owing to the
 482 presence of a distinct alignment of Au–Pd droplets in the
 483 cylinder, 200 μm behind the front. In the upper half of the
 484 capsules, the upper face of the forsterite cylinder underwent
 485 dissolution (see below) and large, euhedral forsterite crystals
 486 grew at the top of the capsules (Figs. 6a, 7a). These crys-
 487 tals are ≈ 100–800 μm in size. They have euhedral outlines,
 488 with planar faces and sharp edges; some of them show large
 489 embayments and contain glass inclusions (Fig. 6c). Large
 490 euhedral crystals are actually present in all experiments of
 491 A and B types (Figs. 3, 4, 5, 6, 7, S3 and S4). In all cases,
 492 they are located at the top of the capsule, which is the coldest

part of the system. In experiment A2, they are not right at the top, but just below a layer of clinopyroxene + spinel + glass, which occupies the upper part of the capsule (Fig. 6a).

Type A experiments show a very special kind of dissolution texture: in experiments A2 and A4, the upper face of the forsterite cylinder displays vertical pillars standing several hundreds of microns above a slightly wavy floor (Figs. 6b, 7b). There is no doubt that these pillars represent a dissolution texture because we found some Au–Pd droplets kept at the top of the pillars or hanging on their walls (Fig. 7e; they are absent in run A2, in which the forsterite cylinder had not been sputtered with Au–Pd), and because the forsterite making the pillars has low levels of CaO and Al₂O₃, which approach the levels of the starting synthetic forsterite and which are lower than those measured in forsterite grown from the haplobasaltic melt (see below). In addition, all overgrowth layers show a very distinct alignment of entrapped Au–Pd droplets underlining the original forsterite surface (for example, sample A4 in Fig. 7c); as we do not see any Au–Pd droplets entrapped at the basis of the pillars in

Fig. 7b, the forsterite pillars are not growth textures. There is also a geometrical argument because the initial position of the upper face of the cylinder is marked by a kink in the platinum wall (Figs. 6a, 7a); the vertical pillars are well inside the original outline of the forsterite cylinders. Finally, we observe that small forsterite crystals (from the starting material) are present in the glass above the dissolution zone, but not in the dissolution zone between the pillars (e.g., the “gulfs” in Fig. 6b).

We prepared a cross section through the layer of forsterite pillars and glass of sample A2 (Fig. 6e). In the center of the sample, the pillars form numerous, sub-rounded sections isolated in glass with $\sim 35 \mu\text{m}$ diameter and a density of 254 pillars per mm^2 (Fig. 6e). Toward the rim, the forsterite increases in proportion relative to glass and it forms polyhedral sections or rods. It is important to note that the forsterite sections from all sides of the capsule display the same crystallographic orientation, which demonstrates that all these crystal units correspond to the same initial forsterite crystal before dissolution. In addition to the forsterite pillars in experiments A2 and A4, a few pillars are also observed in experiment B6 (Fig. 3a, b). Given the crystallographic orientations of the forsterite cylinders in these experiments, the pillars are all elongated preferentially along the a -axis of forsterite.

Mineralogical stratification and temperature gradient

The presence of Sp or Sp + Cpx (in addition to Fo + melt) primarily depends on the nominal temperature of the experiment (1400 or 1425 °C) and on the length of the capsule (3.1–5.1 mm; Table 4). Clinopyroxene was only found

at the top of experiment A2 (Fig. 6), which was made at 1400 °C with a capsule length $> 5 \text{ mm}$. Thus, this combination resulted in a temperature lower than 1330 °C at the very top of the capsule. A few small Sp crystals, but no Cpx, were observed in the layer of large euhedral forsterites at the top of experiments B1 and A4, indicating a temperature lower than 1385 °C but higher than 1330 °C. Again, the presence of an additional phase is related to the length of the samples (4.5 mm). In all other experiments (B6–B9), the capsule length was $< 4.3 \text{ mm}$, and the only solid phase was forsterite even when the nominal temperature was 1400 °C. If we take into account the temperature difference between the thermocouple reading and the maximum temperature at the hot spot (Watson et al. 2002), the temperature interval in these experiments was $< 35 \text{ °C}$ (Table 4).

Chemical results

Chemical compositions of forsterite are presented in Fig. 8a and Table 2. Three main populations can be identified: compositions similar to the starting forsterite, compositions in equilibrium with the haplobasaltic melt at experimental conditions and intermediate ones. The starting forsterite is characterized by a molar ratio Mg/Si of about 1.99, and negligible levels of CaO and Al_2O_3 ($< 0.02 \text{ wt}\%$). The population similar to the composition of starting forsterite has CaO and Al_2O_3 concentrations lower than 0.05 wt% and corresponds to the inner parts of forsterite cylinders, from the interface on the dissolution side to the initial forsterite–melt interface revealed by the alignment of Au–Pd droplets (Figs. 3, 7, 8a). The equilibrium forsterite composition is best represented by the small forsterite grains in experiments such as A4, which have an average Mg/Si ratio of 1.98 and concentrations of

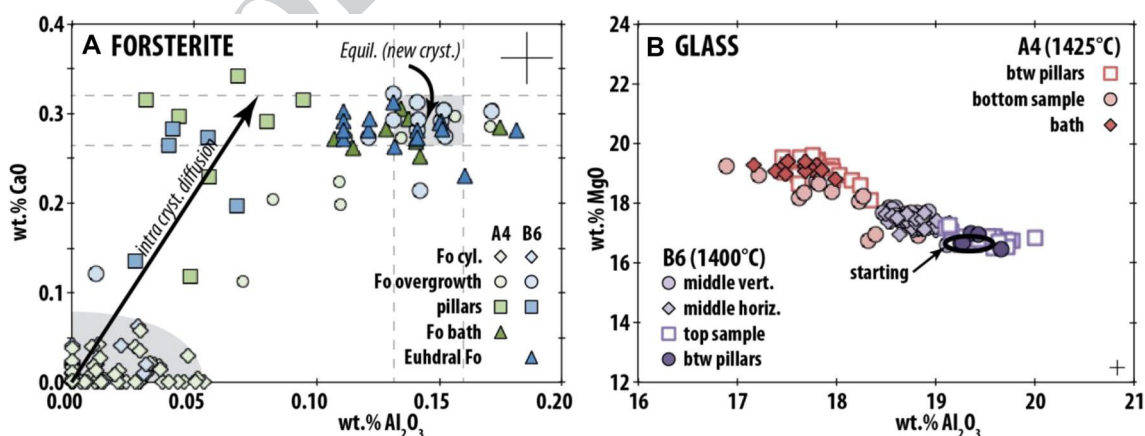


Fig. 8 **a** Diagram CaO vs. Al_2O_3 showing the composition of forsterite in experiments A4 and B6. “Equil. (new cryst.)” corresponds to CaO and Al_2O_3 concentrations in equilibrium with the haplobasalt used here, according to partition coefficients in the literature (Libourel 1999; Pack and Palme 2003). **b** Diagram MgO vs. Al_2O_3

showing glass compositions in experiments A4 and B6. The location of analyses is shown in Figs. 3 and 7. Quench crystallization of forsterite at the end of the experiments led to glass compositions locally strongly depleted in MgO and enriched in Al_2O_3 (see also Fig. 9)

CaO and Al₂O₃ equal to ~0.30 and 0.15 wt%, respectively (Table 2). These relatively large concentrations are typical of forsterite in equilibrium with basaltic melts at high temperatures (Libourel 1999). For Al₂O₃, the data in sample A4 yield a forsterite/liquid partition coefficient of ~0.01, consistent with values of 0.003–0.02 reported by (Pack and Palme 2003) (Fig. 8a). The layers of forsterite overgrown on the initial cylinders and the large, euhedral forsterite crystals are also in equilibrium with the haplobasaltic melt.

The intermediate population of forsterite compositions is associated with the pillars in the dissolution zones, with CaO concentrations approaching the equilibrium defined above and low aluminum contents (<0.10 wt%; Fig. 8a). In fact, there is a gradient from the inner parts of the pillars, which have very low levels of CaO and Al₂O₃ (down to 0.12 wt% and 0.03 wt%, respectively; Table 2) to the rims in contact with haplobasalt, which contain significant concentrations of these two oxides, especially CaO (Fig. S5). The low levels of CaO and Al₂O₃ in the inner parts of the pillars are a strong argument for an origin of this special texture by dissolution. The enrichment in CaO and Al₂O₃ in the outer parts is presumably due to a process of reequilibration with the surrounding melt, with CaO diffusing faster than Al₂O₃ in the forsterite crystalline lattice. The effect of solid-state diffusion can also be observed along profiles performed across the Au–Pd droplet alignments (Fig. 9a); the CaO concentration profiles measured in B6 and A4 experiments show different slopes that are consistent with the run durations. The dissolution side of forsterite cylinders is also likely to be affected by calcium diffusion up to ~80 μm from the melt.

Glass compositions analyzed in experiments A4 and B6 are shown in Fig. 8b. The interpretation of glass compositions is complicated by the late crystallization of forsterite during the quench, which results in a strong depletion of MgO (down to 14 wt%) and enrichment in CaO and Al₂O₃ (Fig. 8b). In fact, MgO depletion is observed over a thickness of several tens of micrometer wherever the glass is in contact with forsterite and is particularly visible in tubes on the precipitation side and in gulfs close to pillars on the dissolution side of forsterite cylinders (e.g., Fig. 7d–e). Putting aside the compositions analyzed close to forsterite, the glass contains in average ≈ 19.1 wt% MgO and 17.8 wt% Al₂O₃ in sample A4, and ≈ 16.8 wt% MgO and 19.5 wt% Al₂O₃ in sample B6 (Table 1). Glass B6 is close to the starting glass (16.4 wt% MgO and 19.4 wt% Al₂O₃) whereas glass A4 is strongly enriched in MgO and depleted in Al₂O₃ in comparison to the starting glass, indicating bulk forsterite dissolution during this experiment. The difference in glass compositions between A4 and B6 is due to the difference in temperature: 1400 °C in run B6 vs. 1425 °C in run A4. Accordingly, the average MgO content in melt increases by 2–2.5 wt% for a temperature increase of 25 °C, that is, a variation of 0.08–0.1 wt% MgO/ °C.

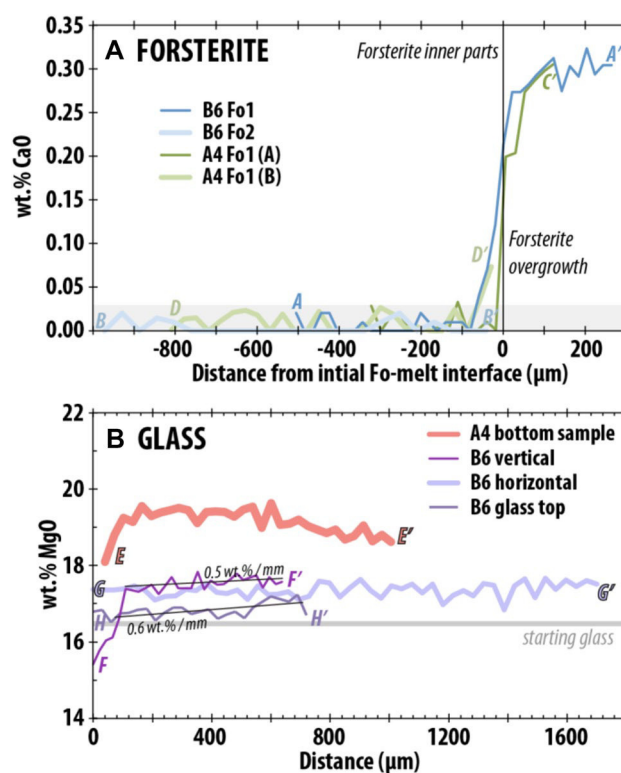


Fig. 9 a Chemical profiles (CaO) of forsterite in A4 and B6 vs. distance from the face of the cylinder at the beginning of the experiment (marked by Au–Pd sputtering). b Chemical profiles (MgO) in the glass in experiments A4 and B6 vs. distance. The concentration of the starting glass is indicated. See Figs. 3 and 7 for the location of the chemical profiles

The melt inclusions of experiments A2, A4 and B1 are texturally homogeneous with no crystals discerned but chemical mapping reveals a heterogeneous distribution of calcium or magnesium (Figs. 6d, 7d). Chemical gradients in glass inclusions are due to crystallization of the host forsterite during the quench. Even the cores of the glass inclusions yield compositions depleted in MgO (8.5–14 wt%; Table 1) in comparison to the compositions measured far from any forsterite. Accordingly, they do not reflect equilibrium conditions. Based on the compositions of forsterite, equilibrium glass composition, and glass in the melt inclusion of experiment A4 (Fig. 7a), we estimate that about 24 wt% of the melt inclusion crystallized during the quench, forming a layer of forsterite a couple of microns thick along the walls.

Rates of dissolution and growth

The growth rate (v_{Growth} , m/s) of the cylinders was determined from the maximum thickness of the growth layer (beyond the Au–Pd sputtering line) divided by run duration (Fig. 10). Similarly, the growth rate of euhedral crystals was calculated by dividing the mean size of the largest crystals

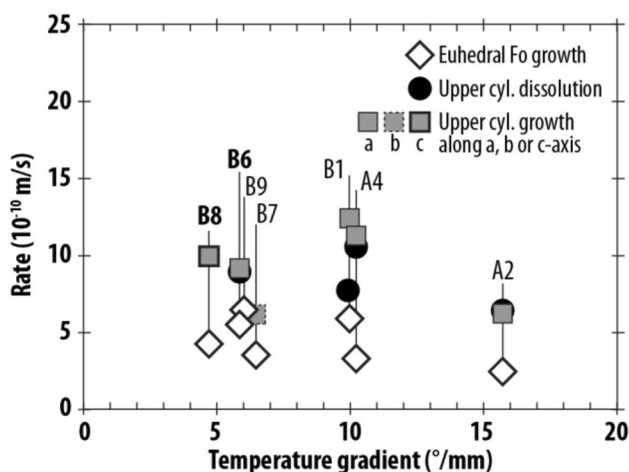


Fig. 10 Growth and dissolution rates of the forsterite cylinder plotted as a function of temperature gradient. The growth rate of large, euhedral forsterite crystals is also shown

by time. To estimate the dissolution rate, we computed the thickness of the dissolution layer as the initial cylinder thickness plus the thickness of the growth layer minus the final cylinder thickness. The thickness of dissolved forsterite can always be closely confirmed by measuring the distance between the final position of the cylinder surface and its initial position marked by the kinks of the capsule wall due to shrinkage, assuming no displacement of the cylinder. In type B experiments, only the upper cylinder was characterized so, because it gives access to both dissolution and growth. The growth rates and dissolution rates range from 5.0×10^{-10} to 1.2×10^{-9} m/s (Table 4; Fig. 10). The growth rate of large, euhedral forsterite ranges from 2×10^{-10} to 7×10^{-10} m/s.

Discussion

Thermal migration as a technique to study growth and dissolution of crystals in silicate liquids

We were able to produce regular growth or dissolution layers reaching thicknesses up to 400 μm by placing monocrySTALLINE cylinders of forsterite into a haplobasaltic melt in a temperature gradient. Of the two experimental configurations tested (Fig. 2a, b), type B involving a layer of melt sandwiched between two forsterite cylinders is by far the more suitable for a quantitative study (Fig. 1). The main advantage is that the transport step of the dissolution/precipitation process is straightforward in comparison to type A experiments, in which the dissolved forsterite components have to find their way between the cylinder wall and the capsule. A potential improvement for the future would be to use forsterite cylinders whose faces correspond to natural faces of olivine phenocrysts. Our experiments show, however, that

similar growth and dissolution textures develop on starting surfaces with different crystallographic orientations. Sputtering a thin layer of Au–Pd over the cylinder faces is of great help to locate the initial forsterite–melt interfaces and to quantify the thickness of the growth layers. Since the same textures are observed in experiments with and without sputtering, the thin layer of gold–palladium does not seem to disturb the dissolution/precipitation processes as long as experiments are run at temperature above the melting point of Au–Pd.

As discussed in “Introduction”, thermal migration encompasses two diffusion potentials that operate simultaneously: saturation gradient chemical diffusion and Soret diffusion. To evaluate the relative importance of these two components, we computed separately the variations of melt composition arising from Soret effect and saturation gradient. Using the Soret coefficients for SiO_2 , Al_2O_3 , MgO , CaO and Na_2O determined experimentally for a MORB composition (Leshner and Walker 1988; Walker and Agee 1988), the composition of melt in experiment B6 (16.81 wt% MgO ; Table 1), and considering two points separated by 1 $^\circ\text{C}$, we obtain a variation of MgO equal to 0.45×10^{-3} in molar fraction (or a variation of 0.03 wt% MgO). This is almost three times smaller than the variation of MgO due to saturation: 1.19×10^{-3} in mole fraction per $^\circ\text{C}$ (based on the difference in liquid compositions in the experiments at 1400 and 1425 $^\circ\text{C}$, B6 and A4, respectively). Accordingly, the dominant process in our thermal migration experiments is saturation gradient chemical diffusion, but Soret effect is not negligible.

The total flux, J (in moles per unit area per unit time), associated with thermal migration is (Leshner and Walker 1988; Walker and Agee 1988)

$$J = -D \frac{dc}{dz} - D' c \frac{dT}{dz}, \quad (1)$$

where the first term on the right-hand side is the flux arising from saturation gradient chemical diffusion, and the second term is the flux arising from the temperature gradient alone. Parameters are as follows: D (cm^2/s), chemical diffusivity; D' ($\text{cm}^2/\text{s}/^\circ\text{C}$), thermal diffusion coefficient; c (mol/cm^3), solute concentration; z (cm), position along the diffusion axis; T ($^\circ\text{C}$), temperature. Introducing the Soret coefficient $\sigma = D'/D$ ($^\circ\text{C}^{-1}$), Eq. (1) can be rewritten:

$$J = -D \frac{dc}{dz} + \sigma c \frac{dT}{dz}, \quad (2)$$

where $[dc/dT]_{\text{Liq}}$ is the variation of concentration with temperature along the liquidus. Equation (2) shows that the flux J is directly proportional to the temperature gradient and is constant as long as the saturation relations and temperature remain unchanged (Leshner and Walker 1988; Walker and Agee 1988).

728 In our experimental configuration (Fig. 1), there is a
 729 direct relationship between the upward flux of MgO by
 730 thermal migration, J_{MgO} , and the growth rate of the upper
 731 forsterite cylinder:

732
$$v_{Growth} = \frac{1}{2} J_{MgO} V_{Fo}, \quad (3)$$

733 where v_{Growth} is the growth rate (cm/s) and V_{Fo} is the molar
 734 volume of forsterite ($\approx 46 \text{ cm}^3/\text{mol}$ in our experimental con-
 735 ditions; (Li et al. 2007)). Thus, if as expected, the flux is
 736 time independent, then the growth rate of forsterite remains
 737 constant during a thermal migration experiment. Using the
 738 relation $c = mp/M$, where m is the mass fraction of an oxide,
 739 M its molar mass, and ρ is the liquid density (assumed con-
 740 stant: 2.7 g/cm^3), we can recombine (1) and (3) into

741
$$\frac{2v_{Growth}}{V_{Fo}} = -\frac{D_{MgO} \rho}{M_{MgO}} \left(\frac{dm_{MgO}}{dz} + \sigma_{MgO} m_{MgO} \frac{dT}{dz} \right). \quad (4)$$

742 For experiment B6, we have $v_{Growth} = 9.4 \times 10^{-8} \text{ cm/s}$,
 743 $m_{MgO} = 0.1681$, $dm_{MgO}/dz = -0.05 \text{ cm}^{-1}$ (Fig. 9b), $dT/$
 744 $dz = -58 \text{ }^\circ\text{C/cm}$ (Table 4); the Soret coefficient σ_{MgO} is
 745 equal to 0.00239 (Leshner and Walker 1988; Walker and
 746 Agee 1988). Thus, we obtain a chemical diffusivity D_{MgO}
 747 equal to $7.8 \times 10^{-7} \text{ cm}^2/\text{s}$, which is in good agreement with
 748 the chemical diffusivity estimated from previous thermal
 749 migration experiments run at conditions close to ours: $D \approx$
 750 $10^{-6} \text{ cm}^2/\text{s}$ (Walker et al. 1988).

751 **Dissolution and growth of forsterite**
 752 **in a temperature gradient**

753 The eight experiments of this study yielded qualitatively
 754 similar dissolution and growth textures: a planar or slightly
 755 wavy forsterite–melt interface, residual pillars (mostly in
 756 type A experiments), and rounded cylinder edges in dis-
 757 solution areas; fingered forsterite–melt interfaces with melt
 758 tubes and melt inclusions in the growth areas. We, therefore,
 759 conclude that these textures are independent of temperature
 760 over the small range investigated (1400–1425 $^\circ\text{C}$; Table 3),
 761 forsterite over glass ratio (in the range 0.25–0.83; Table 3),
 762 and run duration (no qualitative difference between experi-
 763 ments A2 and A4 conducted for 176 and 48 h, respectively).

764 Concerning the dissolution textures, the smooth
 765 melt–crystal interfaces and rounded cylinder edges produced
 766 here are similar to textures described in previous experi-
 767 mental work (Zhang et al. 1989; Donaldson 1990; Soulié
 768 et al. 2017). The pillars represent, however, an original
 769 texture undocumented in the literature to our knowledge,
 770 and do not follow the rule that olivine dissolution produces
 771 almost perfect planar interfaces (Zhang et al. 1989; Chen
 772 and Zhang 2008). We suggest the following scenario. At the
 773 beginning of the experiment, the upper face of the cylinder

was at the level of the tops of the pillars. Because of its
 higher temperature relative to the upper part of the capsule,
 it began to dissolve and recede. With time, the original face
 retreated several hundred micrometers except in areas that
 were somehow protected from dissolution and that gave rise
 to the vertical pillars. As the most characteristic pillars are
 found in runs A2 and A4, the presence of suspended crys-
 tals above the forsterite cylinder is presumably the reason
 why some areas have remained immune to dissolution. As a
 matter of fact, a number of pillars are capped by a small for-
 sterite grain (at the center of Fig. 6b, or on the right side of
 Fig. 7b), and thus resemble the so-called fairy chimneys. In
 contrast, type B experiments, in which there were no crystals
 in suspension above the forsterite cylinder, show dissolution
 surfaces almost perfectly planar with only rare pillars or no
 pillars at all.

Most pillars are robust structures: their length increases
 with time (by dissolution of the neighboring forsterite) since
 they are best developed in the longest duration experiment
 (A2). Some pillars may, however, become unstable with
 time. For instance, there are a few short pillars in Fig. 6b
 that may be in the process of resorption. At this stage, our
 experimental database is not sufficient to establish any sys-
 tematic relationship between the width or the spacing of the
 pillars and the experimental parameters (time, temperature,
 crystal orientation).

Melt composition on the dissolution
and precipitation sides of forsterite cylinders

During the experiments, the melt in contact with forsterite
 is anticipated to be slightly enriched in MgO and depleted
 in CaO and Al_2O_3 (in comparison to the average melt com-
 position) on the dissolution side of forsterite cylinders, and
 slightly depleted in MgO and enriched in CaO and Al_2O_3
 on the precipitation side. We do not have access to the equi-
 librium glass composition at the contact with forsterite due
 to the effect of quench crystallization. To circumvent this
 difficulty, we acquired three EPMA profiles in experiment
 B6 (FF', GG', and HH'; Fig. 3a and Online supplementary
 Table). Profile GG' is a nearly horizontal profile in the melt
 layer between the two forsterite cylinders, and is rather flat
 (Fig. 9b). Profiles FF' and HH' are vertical and extend from
 a zone of forsterite growth to a zone of forsterite dissolu-
 tion. If we ignore the effect of quench crystallization (well
 visible for instance close to F), we observe that the MgO
 content in the glass increases very slightly with a gradient
 of about 0.5–0.6 wt% MgO per mm from the growth side
 to the dissolution side (Fig. 9b). Due to the effect of quench
 crystallization, it is not possible to know the exact MgO
 levels at the contact with the two forsterite cylinders, but the
 difference in MgO between the dissolution and growth sides
 is of the order of 0.35 wt%. Considering a variation of 0.08

Author Proof

825 to 0.1 wt% MgO/ °C for melt in equilibrium with forsterite
 826 (see above), this difference of 0.35 wt% MgO corresponds
 827 to a temperature difference $\Delta T \approx 4$ °C, in good agreement
 828 with the temperature gradient in experiment B6 (5.8 °C/
 829 mm; Table 4) and the thickness of the melt layer (640 μm).
 830 Accordingly, the well-developed growth layer on the lower
 831 face of the upper forsterite cylinder and the thick dissolu-
 832 tion layer on the upper face of the lower cylinder formed
 833 at degrees of undercooling and superheating, respectively,
 834 of ≈ 2 °C ($\Delta T/2$).

835 Cellular growth of olivine in basaltic melts

836 During the solidification of a melt, solid–melt interfaces
 837 become unstable with increasing growth rate, evolving
 838 from planar, to cellular, to dendritic. Cellular growth, which
 839 occurs at low to intermediate growth rates, is well known in
 840 metallurgy (Tiller et al. 1953; Shechtman et al. 1984), but
 841 poorly documented in silicate systems and natural magmas.
 842 Vermiform rims on spinel in natural basalts were interpreted
 843 as the result of a cellular growth mechanism, when diffu-
 844 sion in the melt is no longer able to support the growth of
 845 a smooth interface, creating protuberances (Roeder et al.
 846 2001). Takei and Kobayashi suggested that cellular growth
 847 was responsible for the shape and distribution of minute gas
 848 bubbles in the core of large forsterite monocrystals grown
 849 under a cooling rate of 300 °C/h (Takei and Kobayashi
 850 1974). With the exception of this reference, cellular mor-
 851 phology is absent from the catalog of olivine shapes and
 852 from the classical sequence from polyhedral, tabular, skel-
 853 etal to dendritic shape with increasing degree of undercool-
 854 ing and cooling rate (Donaldson 1976; Faure et al. 2003a).

855 Our experiments show that cellular growth may be a
 856 major growth mechanism for olivine at low to moderate
 857 degrees of undercooling (of the order of 2 °C in experi-
 858 ment B6, for instance) and growth rates of $\approx 10^{-9}$ m/s. The
 859 textures produced support the breakdown of a planar forst-
 860 erite–melt surface into a series of lobes, but we could not
 861 relate the number, frequency or shape ratio of lobes to any
 862 experimental parameter. We note, however, that cellular
 863 growth occurs on surfaces with a lateral extension greater
 864 than 1 mm (1.1 mm in experiment A4, and about 2 mm in
 865 most cases). In comparison, the large euhedral forsterites
 866 whose faces have a lateral extension of at most 300 μm , and
 867 more commonly of the order of 100 μm , display a planar
 868 morphology (Fig. 3b). This contrast is consistent with the
 869 average spacing of lobes (≈ 100 μm). Therefore, cellular
 870 growth seems to require a minimum lateral extension of the
 871 olivine–melt interface of the order of 1 mm. The formation
 872 of a boundary layer enriched in the incompatible elements
 873 rejected by the growing crystal and not able to diffuse away
 874 fast enough could locally impede or slow down the crystal-
 875 lization and, beyond a certain value of the growth rate, cause

the switch from a planar growth front to a cellular morphol- 876
 ogy (Jackson 2004). 877

878 The rates of dissolution and crystallization of forsterite
 879 cylinders and euhedral forsterites are limited to a narrow
 880 range (4×10^{-10} – 1.4×10^{-9} m/s; Table 4). Those values
 881 are very close to the growth rate observed for olivine with a
 882 undercooling of 15 °C (2×10^{-9} m/s) and to the one assessed
 883 for lower undercooling values [6.3×10^{-10} m/s; (Jambon
 884 et al. 1992)]. They fit into the range of natural growth rates
 885 determined for olivines from Etna basalt [2×10^{-11} m/s;
 886 (Armienti et al. 1994)] and from Lanzarote [$\sim 3 \times 10^{-7}$ m/s;
 887 (Armienti et al. 1991)] without and with a 30 °C under-
 888 cooling, respectively, and for olivine from an oceanic basalt
 889 quickly chilled against sediments [3.2×10^{-9} m/s; (Don-
 890 aldson 1975)], although these values were determined by
 891 postmortem observation of the crystal size distribution. They
 892 are slower by half an order of magnitude than the growth
 893 rates measured in situ by (Ni et al. 2014) on olivine. In con-
 894 trast, the growth rates in our study are similar to the ones
 895 measured during transcrystalline migration of melt inclu-
 896 sions within olivine at very small degrees of undercooling
 897 (< 1 °C): 3×10^{-10} to 3.2×10^{-9} m/s (Schiano et al. 2006).
 898 Both our experiments (Fig. 5b) and transcrystalline melt
 899 migration experiments produced (001) faces that are char-
 900 acteristic of a polyhedral olivine habit at very low degrees 901
 of undercooling (Deer et al. 1962). Morphologies with (001) 902
 faces are also observed on olivine dendrites re-equilibrated 903
 under near equilibrium conditions (Faure et al. 2003b). The 904
 slow growth rate, the absence of marked chemical gradients 905
 at crystal–liquid interfaces and the presence of (001) faces 906
 are evidence of very low degrees of undercooling during 907
 experiments. 908

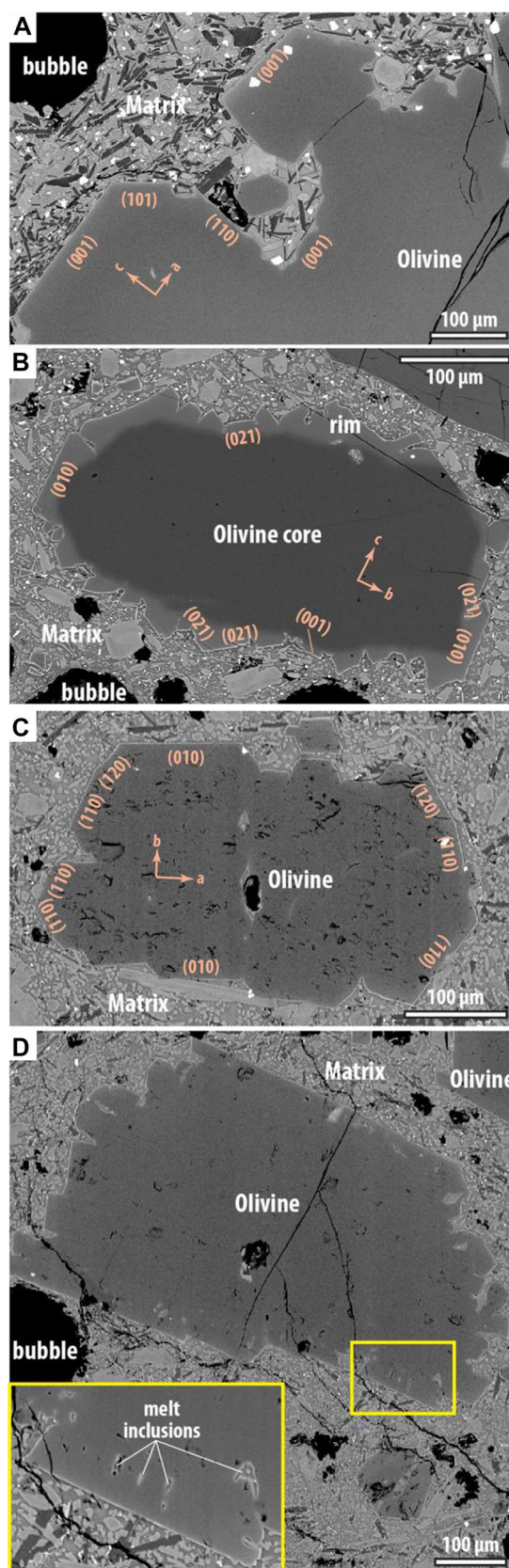
909 Faure et al. retained four main morphologies of olivine
 910 among the ten described by Donaldson (1976): polyhedral,
 911 tabular, hopper and dendritic (Faure et al. 2003a). Those
 912 morphologies depend on the type of growth mechanism,
 913 steady-state vs. rapid growth mechanisms, which depends,
 914 in turn, on the cooling rate and the degree of undercool-
 915 ing (Faure et al. 2003a). Here, we show a new type of
 916 growth mechanism, cellular growth, and new growth
 917 morphologies that have not been described in previous
 918 studies, in which olivine growth was investigated using
 919 cooling experiments (Donaldson 1975, 1976; Coish and
 920 Taylor 1979; Kirkpatrick 1981; Lofgren 1983; Jambon
 921 et al. 1992; Faure et al. 2003a; Faure and Schiano 2005;
 922 Welsch et al. 2012; Ni et al. 2014). Compared to classical
 923 cooling experiments, our thermal migration experiments
 924 allow to combine two parameters that are required for the
 925 occurrence of cellular growth and for the development
 926 of cellular morphologies: low degrees of undercooling
 927 (estimated at 2 °C in experiment B6) and large forst-
 928 erite–melt interfaces (typically 2 mm in diameter). Based on
 our experiments, the classical degree of undercooling vs.

Fig. 11 SEM images showing microtextures suggestive of cellular overgrowth in natural olivine phenocrysts from the basanitic tephra of **a** Montcineyre volcano (Chaîne des Puys, France), **b** Souilhol volcano (Ardèche, France), and **c, d** Thueyts volcano (Ardèche). The core of the crystal in **b** is a xenocryst of MgO-rich composition, which is completely surrounded by lobes of olivine in equilibrium with the basanitic matrix. The crystallographic orientation is indicated in pink font

929 cooling rate vs. olivine morphologies scheme (Faure et al.
 930 2007) needs to be completed to include cellular growth of
 931 olivine. Integrating the new data with previous ones, we
 932 are able to link growth texture in olivine to growth rate:
 933 polyhedral, tabular, and cellular morphologies occur at
 934 crystallization rates of $\approx 10^{-9}$ m/s and below, while hop-
 935 per and dendritic morphologies are generated for higher
 936 growth rates ($\approx 10^{-8}$ m/s and $> 10^{-8}$ m/s, respectively)
 937 (Faure et al. 2007; Ni et al. 2014).

Natural occurrences of cellular growth in magmas

938
 939 The main goal of our thermal migration experiments was
 940 to access the low degrees of undercooling characteristic of
 941 most magmatic systems. Under conditions pertaining to
 942 natural systems (low degrees of undercooling and large phe-
 943 nocryt faces), our major finding is the development of cel-
 944 lular morphologies. To date, cellular growth has been poorly
 945 documented in the literature, with few natural examples on
 946 pyroxene, plagioclase and spinel (Singer and Pearce 1993;
 947 Andersson and Eklund 1994; Hibbard and Sjöberg 1994;
 948 Roeder et al. 2001). However, we believe that cellular mor-
 949 phologies are much more frequent and may not have been
 950 detected in the past. For instance, we found microtextures
 951 that are suggestive of cellular growth in olivines from the
 952 basanitic tephra of Montcineyre (Chaîne des Puys, France;
 953 Fig. 11a) and Souilhol and Thueyts volcanoes (Ardèche,
 954 France; Fig. 11b–d). The olivine phenocrysts are a few mm
 955 long at Montcineyre, and between 0.5 and 1 mm at Souil-
 956 hol and Thueyts. Most olivine phenocrysts in these basan-
 957 ites are characterized by a discontinuous outer part show-
 958 ing lobes or blocks of growth separated by depressed areas
 959 or embayments: the result is a crenulated outline. Olivine
 960 xenocrysts, which are frequent in these basanites, show the
 961 same morphology at their periphery; the MgO-rich olivine
 962 core in Fig. 11b is completely surrounded by lobes of olivine
 963 in equilibrium with the basanitic matrix. Small melt inclu-
 964 sions are found in the rim of some olivines from Thueyts
 965 (Fig. 11d), yielding microtextures reminiscent of a process
 966 of cellular growth in which neighboring lobes merged at
 967 their ends and entrapped melt droplets at their roots. In the
 968 examples of Fig. 11, the final stage of olivine growth was
 969 frozen by the eruption, allowing the preservation of what we
 970 interpret as textures of cellular growth.



971 **Constraints on melt inclusion formation**

972 A possible consequence of crystal growth is the entrapment
 973 of melt inclusions. With the experimental configuration
 974 used here, we could test for the necessity of a temperature
 975 decrease to form melt inclusions, such as suggested by Gold-
 976 stein and Luth (2006) who produced inclusions at cooling
 977 rates higher than 1 °C/h only. Here, we generated melt inclu-
 978 sions resembling natural ones in the absence of temperature
 979 variations, but with temperature gradients of a few degrees
 980 per mm which drove olivine growth under low degrees of
 981 undercooling. Therefore, melt inclusions can be formed in
 982 steady P–T systems at low degrees of undercooling; their
 983 formation does not require a specific cooling regime or rapid
 984 crystallization (skeletal of dendritic growth) as previously
 985 proposed (Albarede and Bottinga 1972; Roedder 1979; Wat-
 986 son 1996; Schiano 2003; Kohut and Nielsen 2004; Faure
 987 and Schiano 2005; Goldstein and Luth 2006; Faure et al.
 988 2007). Cellular growth could favor the formation of melt
 989 inclusions by giving rise to melt tubes that will subsequently
 990 get closed at their ends (Higuchi et al. 1995; Nakamura and
 991 Shimakita 1998; Colin et al. 2012). This process is well
 992 illustrated by the merging of neighboring lobes terminated
 993 by crystallographic facets in experiment B6 (Fig. 3c), and
 994 closely resembles the mechanism described by Colin et al.
 995 in skeletal olivine crystals found in a MORB (Colin et al.
 996 2012). However, we do not claim that our experiments rep-
 997 resent the unique or the most likely way of making inclu-
 998 sions, and there is natural and experimental evidence that
 999 melt inclusions form under varying pressure and/or tem-
 1000 perature (Kohut and Nielsen 2004; Faure and Schiano 2005;
 1001 Faure et al. 2007; Manzini et al. 2017). Cellular growth is
 1002 another mechanism to generate melt inclusions hosted in
 1003 polyhedral forsterite, in addition to the interaction between
 1004 spiral growth dislocations (Faure and Schiano 2005), par-
 1005 tial dissolution of host mineral followed by recrystallization
 1006 (Anderson 1991; Nakamura and Shimakita 1998; Welsch
 1007 et al. 2014; Manzini et al. 2017), dissolution of preexist-
 1008 ing crystals or impurities (Davey and Mullin 1974; Michael
 1009 et al. 2002), or fluctuation of growth rate (Roedder 1979).

1010 **Conclusions**

1011 We used an original experimental setup based on thermal
 1012 migration to monitor the growth of large forsterite cylinders
 1013 (single crystals) at low degrees of undercooling (≈ 2 °C).
 1014 As forsterite solubility is sensitive to temperature, the
 1015 temperature gradient within the capsules generated a dis-
 1016 solution–precipitation process involving (1) dissolution
 1017 of forsterite on the high-temperature side (giving rise to
 1018 rounded crystal–melt interfaces and pillars of residual for-
 1019 sterite); (2) transport of dissolved components in the melt;

(3) precipitation on the low-temperature side (giving rise to
 thick layers of newly grown forsterite with a fingered inter-
 face and melt inclusions, and to the growth of large, euhe-
 dral crystals of forsterite). The starting forsterite cylinders
 were sputtered with Au–Pd allowing us to mark the initial
 melt–forsterite interface and to quantify crystal growth.

The fingered crystal–melt interfaces observed on the
 crystallization side of forsterite cylinders result from cel-
 lular growth, a type of growth that had not been produced
 experimentally so far in silicate systems. Our experiments
 show that cellular growth requires a low degree of under-
 cooling (a few °C) and a large substrate (~ 1 mm across
 or more), and that it occurs at growth rates of the order of
 10^{-9} m/s. Cellular growth can lead to the formation of melt
 inclusions at relatively slow rates of growth. Although
 we found microtextures suggestive of cellular growth in
 olivines from mafic rocks of the French Massif Central,
 cellular textures are poorly documented in natural prod-
 ucts, probably because they were not recognized as such.

Acknowledgements The authors acknowledge the technical assis-
 tance of Jean-Luc Devidal, Jean-Marc Hénot, Franck Pointud, Antoine
 Mathieu, Jean-Louis Fruquière and Cyrille Guillot. Denis Andraut
 is thanked for stimulating discussions, Manon Hardiagon for sharing
 her unpublished data on the composition and phase diagram of the
 Na-CMAS starting glass, and Vladimir Antonoff for his help in the
 temperature calibration experiments. This research was financed by
 the French Government Laboratory of Excellence initiative number
 ANR-10-LABX-0006, Région Auvergne and the European Regional
 Development Fund. This is Laboratory of Excellence ClerVolc
 contribution number 359. We thank Y. Liang and Y. Zhang for their con-
 structive reviews.

References

- Albarede F, Bottinga Y (1972) Kinetic disequilibrium in trace ele-
 ment partitioning between phenocrysts and host lava. *Geochim
 Cosmochim Acta* 36:141–156
- Anderson AT Jr (1991) Hourglass inclusions: theory and application
 to the Bishop Rhyolitic Tuff. *Am Mineral* 76:530–547
- Andersson UB, Eklund O (1994) Cellular plagioclase intergrowths as
 a result of crystal–magma mixing in the Proterozoic Aland rapa-
 kivi batholith, SW Finland. *Contrib Mineral Petrol* 117:124–
 136. <https://doi.org/10.1007/BF00286837>
- Armienti P, Innocenti F, Pareschi MT et al (1991) Crystal population
 density in not stationary volcanic systems: estimate of olivine
 growth rate in basalts of Lanzarote (Canary Islands). *Mineral
 Petrol* 44:181–196
- Armienti P, Pareschi MT, Innocenti F, Pompilio M (1994) Effects
 of magma storage and ascent on the kinetics of crystal growth.
Contrib Mineral Petrol 115:402–414
- Blundy J, Cashman K, Humphreys M (2006) Magma heating by
 decompression-driven crystallization beneath andesite volca-
 noes. *Nature* 443:76–80. <https://doi.org/10.1038/nature05100>
- Brewer TS (2000) Remobilization of andesite magma by intrusion of
 Ma c magma at the Soufriere Hills Volcano, Montserrat, West
 Indies. *J Petrol* 41:21–42

Author Proof

1074 Buchwald VF, Kjer T, Thorsen KA (1985) Thermal migration: or
 1075 how to transport iron sulfide in solid iron meteorites. *Meteoritics*
 1076 20:617

1077 Cabane H, Laporte D, Provost A (2005) An experimental study of Ost-
 1078 wald ripening of olivine and plagioclase in silicate melts: implica-
 1079 tions for the growth and size of crystals in magmas. *Contrib Miner-
 1080 eral Petrol* 150:37–53. <https://doi.org/10.1007/s00410-005-0002-2>

1081 Castro JM, Dingwell DB (2009) Rapid ascent of rhyolitic magma
 1082 at Chaitén volcano, Chile. *Nature* 461:780–783. <https://doi.org/10.1038/nature08458>

1083
 1084 Chen Y, Zhang Y (2008) Olivine dissolution in basaltic melt. *Geochim
 1085 Cosmochim Acta* 72:4756–4777

1086 Coish RA, Taylor LA (1979) The effects of cooling rate on texture and
 1087 pyroxene chemistry in DSDP Leg 34 basalt: a microprobe study.
 1088 *Earth Planet Sci Lett* 42:389–398

1089 Colin A, Faure F, Burnard P (2012) Timescales of convection in
 1090 magma chambers below the Mid-Atlantic ridge from melt inclu-
 1091 sions investigations. *Contrib Mineral Petrol* 164:677–691

1092 Costa F, Coogan LA, Chakraborty S (2010) The time scales of magma
 1093 mixing and mingling involving primitive melts and melt-mush
 1094 interaction at mid-ocean ridges. *Contrib Mineral Petrol* 159:371–
 1095 387. <https://doi.org/10.1007/s00410-009-0432-3>

1096 Davey RJ, Mullin JW (1974) Growth of the 100 faces of ammonium
 1097 dihydrogen phosphate crystals in the presence of ionic species. *J
 1098 Cryst Growth* 26:45–51

1099 Donaldson CH (1975) Calculated diffusion coefficients and the growth
 1100 rate of olivine in a basalt magma. *Lithos* 8:163–174

1101 Donaldson CH (1976) An experimental investigation of olivine mor-
 1102 phology. *Contrib Mineral Petrol* 57:187–213

1103 Donaldson CH (1990) Forsterite dissolution in superheated basaltic,
 1104 andesitic and rhyolitic melts. *Miner Mag* 54:67–74

1105 Druitt TH, Costa F, Deloule E et al (2012) Decadal to monthly time-
 1106 scales of magma transfer and reservoir growth at a caldera vol-
 1107 cano. *Nature* 482:77–80. <https://doi.org/10.1038/nature10706>

1108 Eppich GR, Cooper KM, Kent AJR, Koleszar A (2012) Constraints
 1109 on crystal storage timescales in mixed magmas: uranium-series
 1110 disequilibria in plagioclase from Holocene magmas at Mount
 1111 Hood, Oregon. *Earth Planet Sci Lett* 317–318:319–330. <https://doi.org/10.1016/j.epsl.2011.11.019>

1112
 1113 Faure F, Schiano P (2005) Experimental investigation of equilibration
 1114 conditions during forsterite growth and melt inclusion formation.
 1115 *Earth Planet Sci Lett* 236:882–898. <https://doi.org/10.1016/j.epsl.2005.04.050>

1116
 1117 Faure F, Trolliard G, Nicollet C, Montel JM (2003a) A developmen-
 1118 tal model of olivine morphology as a function of the cooling rate and
 1119 the degree of undercooling. *Contrib Mineral Petrol* 145:251–263.
 1120 <https://doi.org/10.1007/s00410-003-0449-y>

1121
 1122 Faure F, Trolliard G, Soulestin B (2003b) TEM investigation of forst-
 1123 erite dendrites. *Am Mineral* 88:1241–1250

1124
 1125 Faure F, Schiano P, Trolliard G et al (2007) Textural evolution of poly-
 1126 hedral olivine experiencing rapid cooling rates. *Contrib Mineral
 1127 Petrol* 153:405–416. <https://doi.org/10.1007/s00410-006-0154-8>

1128
 1129 Goldstein SB, Luth RW (2006) The importance of cooling regime in
 1130 the formation of melt inclusions in olivine crystals in haplobas-
 1131 altic melts. *Can Mineral* 44:1543–1555. <https://doi.org/10.2113/gscanmin.44.6.1543>

1132
 1133 Hibbard MJ, Sjöberg JJ (1994) Signs of incongruent melting of clino-
 1134 pyroxene in limburgite, Thetford Hill, Vermont. *Can Mineral*
 1135 32:307–317

1136
 1137 Higuchi M, Geray RF, Dieckmann R et al (1995) Growth of Cr₄+ -rich,
 1138 chromium-doped forsterite single crystals by the floating zone
 1139 method. *J Cryst Growth* 148:140–147

1140
 1141 Humphreys MCS, Blundy JD, Sparks RSJ (2006) Magma evolution and
 1142 open-system processes at Shiveluch Volcano: insights from phe-
 1143 nocrust zoning. *J Petrol* 47:2303–2334. <https://doi.org/10.1093/ptrology/egl045>

1144
 1145 Ito K, Sato H, Kanazawa H et al (2003a) First synthesis of oli-
 1146 vine single crystal as large as 250 carats. *J Cryst Growth*
 1147 253:557–561

1148
 1149 Ito K, Sato H, Takei H, et al (2003b) Synthesis of large high-quality
 1150 forsterite single crystals to 200 mm length and its significance.
 1151 *Geochemistry, Geophys Geosystems* 4

1152
 1153 Jackson KA (2004) Constitutional supercooling surface roughening. *J
 1154 Cryst Growth* 264:519–529

1155
 1156 Jambon A, Lussiez P, Clocchiatti R et al (1992) Olivine growth rate
 1157 in a tholeiitic basalt: an experimental study of melt inclusion in
 1158 plagioclase. *Chem Geol* 96:277–287

1159
 1160 Keith HD, Padden FJ Jr (1963) A phenomenological theory of spheru-
 1161 litic crystallization. *J Appl Phys* 34:2409–2421

1162
 1163 Kirkpatrick RJ (1975) Crystal growth from the melt: a review. *Am
 1164 Miner* 60:798–814

1165
 1166 Kirkpatrick RJ (1981) Kinetics of crystallization of igneous rocks. *Rev
 1167 Miner States* 8

1168
 1169 Kohut E, Nielsen RL (2004) Melt inclusion formation mechanisms
 1170 and compositional effects in high-An feldspar and high-Fo oli-
 1171 vine in anhydrous mafic silicate liquids. *Contrib Mineral Petrol*
 1172 147:684–704. <https://doi.org/10.1007/s00410-004-0576-0>

1173
 1174 Launeau P (2004) Evidence of magmatic flow by 2-D image analysis
 1175 of 3-D shape preferred orientation distributions. *Bull la Société
 1176 Géologique Fr* 175:331–350

1177
 1178 Leshner CE, Walker D (1986) Solution properties of silicate liquids
 1179 from thermal diffusion experiments. *Geochim Cosmochim Acta*
 1180 50:1397–1411

1181
 1182 Leshner CE, Walker D (1988) Cumulate maturation and melt migra-
 1183 tion in a temperature gradient. *J Geophys Res Solid Earth*
 1184 93:10295–10311

1185
 1186 Li L, Wentzcovitch RM, Weidner DJ, Da Silva CRS (2007) Vibrational
 1187 and thermodynamic properties of forsterite at mantle conditions.
 1188 *J Geophys Res Solid Earth* 112:

1189
 1190 Libourel G (1999) Systematics of calcium partitioning between oli-
 1191 vine and silicate melt: implications for melt structure and calcium
 1192 content of magmatic olivines. *Contrib Mineral Petrol* 136:63–80.
 1193 <https://doi.org/10.1007/s004100050524>

1194
 1195 Lofgren GE (1983) Effect of heterogeneous nucleation on basaltic tex-
 1196 tures: a dynamic crystallization study. *J Petrol* 24:229–255

1197
 1198 Manzini M, Bouvier A-S, Baumgartner LP et al (2017) Weekly to
 1199 monthly time scale of melt inclusion entrapment prior to eruption
 1200 recorded by phosphorus distribution in olivine from mid-ocean
 1201 ridges. *Geology* 45:1059–1062

1202
 1203 Michael PJ, McDonough WF, Nielsen RL, Cornell WC (2002)
 1204 Depleted melt inclusions in MORB plagioclase: messages from
 1205 the mantle or mirages from the magma chamber? *Chem Geol*
 1206 183:43–61

1207
 1208 Morgan DJ, Blake S (2006) Magmatic residence times of zoned phe-
 1209 nocrusts: introduction and application of the binary element dif-
 1210 fusion modelling (BEDM) technique. *Contrib Mineral Petrol*
 1211 151:58–70. <https://doi.org/10.1007/s00410-005-0045-4>

1212
 1213 Murphy MD, Sparks RSJ, Barclay J et al (2000) Remobilization of
 1214 andesite magma by intrusion of mafic magma at the Soufriere
 1215 Hills volcano, Montserrat, West Indies. *J Petrol* 41:21–42. <https://doi.org/10.1093/ptrology/41.1.21>

1216
 1217 Nakamura M, Shimakita S (1998) Dissolution origin and syn-entrap-
 1218 ment compositional change of melt inclusion in plagioclase.
 1219 *Earth Planet Sci Lett* 161:119–133. [https://doi.org/10.1016/S0012-821X\(98\)00144-7](https://doi.org/10.1016/S0012-821X(98)00144-7)

1220
 1221 Ni H, Keppler H, Walte N et al (2014) In situ observation of crystal
 1222 growth in a basalt melt and the development of crystal size distri-
 1223 bution in igneous rocks. *Contrib Mineral Petrol* 167:1–13. <https://doi.org/10.1007/s00410-014-1003-9>

1224
 1225 O'hara S, Tarshis LA, Tiller WA, Hunt JP (1968) Discussion of inter-
 1226 face stability of large facets on solution grown crystals. *J Cryst
 1227 Growth* 3:555–561

- 1206 Pack A, Palme H (2003) Partitioning of Ca and Al between forsterite
1207 and silicate melt in dynamic systems with implications for the
1208 origin of Ca, Al-rich forsterites in primitive meteorites. *Meteorit*
1209 *Planet Sci* 38:1263–1281
- 1210 Roedder E (1979) Origin and significance of magmatic inclusions. *Bull*
1211 *Mineral* 102:487–510
- 1212 Roedder E, Bodnar RJ (1980) Geologic pressure determinations from
1213 fluid inclusion studies. *Annu Rev Earth Planet Sci* 8:263–301
- 1214 Roeder PL, Poustovetov A, Oskarsson N (2001) Growth forms and
1215 composition of chromian spinel in MORB magma: diffusion-
1216 controlled crystallization of chromian spinel. *Can Mineral*
1217 39:397–416
- 1218 Schiano P (2003) Primitive mantle magmas recorded as silicate melt
1219 inclusions in igneous minerals. *Earth-Science Rev* 63:121–144.
1220 [https://doi.org/10.1016/S0012-8252\(03\)00034-5](https://doi.org/10.1016/S0012-8252(03)00034-5)
- 1221 Schiano P, Provost A, Clochiatti R, Faure F (2006) Transcrystalline
1222 melt migration and Earth's mantle. *Science* 80(314):970–974
- 1223 Shechtman D, Blech I, Gratias D, Cahn JW (1984) Metallic phase
1224 with long-range orientational order and no translational symmetry.
1225 *Phys Rev Lett* 53:1951
- 1226 Singer BS, Pearce TH (1993) Plagioclase zonation in a basalt to rhyo-
1227 dacite eruptive suite, Seguam Island, Alaska: observations by
1228 Nomarski contrast interference. *Can Mineral* 31:459–466
- 1229 Sonzogni Y, Provost A, Schiano P (2011) Transcrystalline melt migra-
1230 tion in clinopyroxene. *Contrib to Mineral Petrol* 161:497–510.
1231 <https://doi.org/10.1007/s00410-010-0545-8>
- 1232 Soulié C, Libourel G, Tissandier L (2017) Olivine dissolution in molten
1233 silicates: an experimental study with application to chondrule for-
1234 mation. *Meteorit Planet Sci* 52:225–250. [https://doi.org/10.1111/](https://doi.org/10.1111/maps.12792)
1235 [maps.12792](https://doi.org/10.1111/maps.12792)
- 1236 Sunagawa I (1981) Characteristics of crystal growth in nature as
1237 seen from the morphology of mineral crystals. *Bull minéralogie*
1238 104:81–87
- 1239 Takei H, Kobayashi T (1974) Growth and properties of Mg₂SiO₄ single
1240 crystals. *J Cryst Growth* 23:121–124
- 1241 Tiller WA, Jackson KA, Rutter JW, Chalmers B (1953) The redistri-
1242 bution of solute atoms during the solidification of metals. *Acta*
1243 *Metall* 1:428–437
- Viccaro M, Giuffrida M, Nicotra E, Ozerov AY (2012) Magma storage,
1244 ascent and recharge history prior to the 1991 eruption at Avachin-
1245 sky Volcano, Kamchatka, Russia: inferences on the plumbing sys-
1246 tem geometry. *Lithos* 140–141:11–24. [https://doi.org/10.1016/j.](https://doi.org/10.1016/j.lithos.2012.01.019)
1247 [lithos.2012.01.019](https://doi.org/10.1016/j.lithos.2012.01.019)
- Walker D, Agee CB (1988) Ureilite compaction. *Meteoritics* 23:81–91 1248
- Walker D, Jurewicz S, Watson EB (1988) Adcumulus dunite growth in
1249 a laboratory thermal gradient. *Contrib Mineral Petrol* 99:306–319 1250
- Watson EB (1996) Surface enrichment and trace-element uptake during
1251 crystal growth. *Geochim Cosmochim Acta* 60:5013–5020 1252
- Watson E, Wark D, Price J, Van Orman J (2002) Mapping the thermal
1253 structure of solid-media pressure assemblies. *Contrib Mineral*
1254 *Petrol* 142:640–652 1255
- Welsch B, Faure F, Famin V et al (2012) Dendritic crystallization: a
1256 single process for all the textures of olivine in basalts? *J Petrol*
1257 54:539–574 1258
- Welsch B, Faure F, Famin V et al (2013) Dendritic crystallization: a
1259 single process for all the textures of olivine in basalts? *J Petrol*
1260 54:539–574. [https://doi.org/10.1093/](https://doi.org/10.1093/petrology/egs077)
1261 [petrology/egs077](https://doi.org/10.1093/petrology/egs077) 1262
- Welsch B, Hammer J, Hellebrand E (2014) Phosphorus zoning reveals
1263 dendritic architecture of olivine. *Geology* 42:867–870 1264
- Zellmer GF, Sheth HC, Iizuka Y, Lai YJ (2012) Remobilization of
1265 granitoid rocks through mafic recharge: evidence from basalt-
1266 trachyte mingling and hybridization in the Manori-Gorai area,
1267 Mumbai, Deccan Traps. *Bull Volcanol* 74:47–66. [https://doi.](https://doi.org/10.1007/s00445-011-0498-4)
1268 [org/10.1007/s00445-011-0498-4](https://doi.org/10.1007/s00445-011-0498-4) 1269
- Zhang Y, Walker D, Leshner CE (1989) Diffusive crystal dissolution.
1270 *Contrib to Mineral Petrol* 102:492–513. [https://doi.org/10.1007/](https://doi.org/10.1007/BF00371090)
1271 [BF00371090](https://doi.org/10.1007/BF00371090) 1272
- Publisher's Note** Springer Nature remains neutral with regard to
1273 jurisdictional claims in published maps and institutional affiliations. 1274
- 1275